Theor. Comput. Fluid Dyn. (2019) 33:359–382
https://doi.org/10.1007/s00162-019-00498-8

ORIGINAL ARTICLE

Aaron Towne · Georgios Rigas · Tim Colonius

A critical assessment of the parabolized stability equations

Received: 5 July 2018 / Accepted: 6 June 2019 / Published online: 13 June 2019

Abstract The parabolized stability equations (PSE) are a ubiquitous tool for studying the stability and evolution of disturbances in weakly nonparallel, convectively unstable flows. The PSE method was introduced as an alternative to asymptotic approaches to these problems. More recently, PSE has been applied with mixed results to a more diverse set of problems, often involving flows with multiple relevant instability modes. This paper investigates the limits of validity of PSE via a spectral analysis of the PSE operator. We show that PSE is capable of accurately capturing only disturbances with a single wavelength at each frequency and that other disturbances are not necessarily damped away or properly evolved, as often assumed. This limitation is the result of regularization techniques that are required to suppress instabilities arising from the ill-posedness of treating a boundary value problem as an initial value problem. These findings are valid for both incompressible and compressible formulations of PSE and are particularly relevant for applications involving multiple modes with different wavelengths and growth rates, such as problems involving multiple instability mechanisms, transient growth, and acoustics. Our theoretical results are illustrated using a generic problem from acoustics and a dual-stream jet, and the PSE solutions are compared to both global solutions of the linearized Navier–Stokes equations and a recently developed alternative parabolization.

Keywords Parabolized stability equations · Regularization · Error analysis

1 Introduction

The parabolized stability equations (PSE) offer a simple and fast approach to analyzing the linear and nonlinear stability of disturbances in weakly nonparallel, spatially developing flows [5,20]. The low computational cost of PSE compared to fully nonparallel and/or nonlinear methods and its practical simplicity compared to rigorous asymptotic approaches have made it a popular and powerful complement to classical parallel-flow linear stability theory. It has been used fruitfully to study numerous flows, including boundary layers (e.g., [4,27,34]) and free shear flows (e.g., [13,16]).

PSE is designed to track the downstream response to an initial disturbance that is specified at some streamwise location in the flow. The fundamental assumption of PSE is that the majority of the streamwise oscillation and growth of the response at each frequency can be described by a single complex wavenumber that is allowed to vary slowly in the streamwise direction. This assumption leads to a modified flow operator

Communicated by Vassilios Theofilis.

A. Towne (✉)
University of Michigan, Ann Arbor, MI 48109, USA
E-mail: towne@umich.edu

G. Rigas · T. Colonius
California Institute of Technology, Pasadena, CA 91125, USA

which is numerically integrated in the downstream direction to obtain an approximation of the downstream response to the initial disturbance.

In traditional applications of PSE, the initial disturbance is chosen to correspond to a (convectively) unstable eigenmode of the local linearized Navier–Stokes (LNS) operator at a given frequency. The response is then interpreted to represent the weakly nonparallel and/or nonlinear generalization of the local mode. Accordingly, PSE can be viewed as an alternative to earlier asymptotic methods that constructed weakly nonparallel solutions by stitching together a set of local eigenmodes computed at different streamwise locations [6,12,15]. By construction, the solutions obtained from these asymptotic methods are composed entirely of a single slowly varying local eigenmode with a single slowly varying wavenumber—other modes of the LNS operator do not participate.

In contrast, the PSE solution can in principle contain contributions from many local LNS eigenmodes with different wavenumbers, even when just one is selected as the initial disturbance. The reason for this is that the PSE operator supports most of the same eigenmodes as the LNS operator (c.f., Li and Malik [26] or Sect. 2.2 below), and these modes are coupled together through both linear and nonlinear mechanisms. The streamwise variation of the flow leads to slow changes in the LNS eigenfunctions that create a linear coupling between the different local LNS modes at a given frequency. This coupling provides a mechanism for energy transfer from one mode to another; each mode can both leak energy to and acquire energy from other modes as it evolves. Additionally, nonlinear triadic interactions between different frequencies constitute a forcing of the linear dynamics that can potentially excite any LNS mode, not just those with a particular wavenumber.

Ideally, energy that is transferred away from the primary mode described by the PSE wavenumber and into modes with different wavenumbers would be either (i) quickly damped away or (ii) properly evolved by the downstream PSE march. In the first case, the solution would then consist almost exclusively of a single slowly varying eigenmode and the solution could be interpreted as a single weakly nonparallel (and possibly nonlinear) eigenmode. In the second case, the solution could be understood as the full downstream response of the initial perturbation, under the assumption of zero upstream feedback.

In addition to the traditional (modal) usage of PSE described so far, the method has also been used more broadly as a low-cost approximation for the LNS equations. Applications include sensitivity analysis to external forcing [29], optimal spatial transient growth analysis [2,17,28,40], adjoint-based control [46], modeling acoustic emissions [10,37], and predicting flow statistics via stochastic forcing [30]. These applications can involve multiple modes with potentially different wavelengths and growth rates. Examples include flows with multiple unstable modes such as hypersonic boundary layers and multi-stream shear flows, compressible flows in which acoustics are of interest, and any flow susceptible to transient growth, which by definition involves the superposition of multiple modes. Obtaining accurate results for these applications involving multiple modes of interest requires accurately capturing all participating modes, and using PSE in these cases has yielded mixed results, with some authors reporting success (e.g., [17,37]) and others noting limitations and challenges (e.g., [10,33]).

Several alternative methods are available that naturally account for multiple modes with disparate wavelengths. Global methods based on the multi-dimensional LNS operator can capture any wavelength supported by the flow, but these methods are computationally intensive, especially for three-dimensional problems. Alternatively, Towne and Colonius [44] recently introduced a method called one-way Euler (OWE; [42]) or one-way Navier–Stokes equations (OWNS; [31]) for rapidly approximating the LNS solution using a spatial marching procedure much like that of PSE. Using ideas originally developed for constructing high-order nonreflecting boundary conditions, the flow variables are decomposed into upstream and downstream propagating waves, and an approximate evolution equation is derived for the downstream waves. The spatial integration is formally well posed (unlike PSE, see Sect. 2.2) and can capture the downstream-traveling waves with arbitrary accuracy. The method is typically more than an order of magnitude faster than global methods, but still slower than PSE by a similar factor. Because of this speed advantage, PSE remains a valuable tool in cases for which it can deliver sufficient accuracy.

With this motivation, the goal of this paper is to provide an improved understanding of the limits of validity of PSE. In particular, we perform a spectral analysis of the PSE operator to evaluate the ability of PSE to evolve modes whose wavelength and growth rate differ from the primary wave being tracked in the downstream march. The main result of the paper is that, in general, only modes whose eigenvalue lies near the primary PSE wavenumber in the complex plane are accurately evolved by PSE, but other modes present may or may not be damped. While this result seems to already be implicitly understood by some in the community, we make explicit the restrictions and show that they apply to all existing variants of PSE. This implies that PSE will deliver an accurate solution only if the flow, at a given frequency, is dominated by a single wavelength and growth rate, suggesting that great care should be taken when applying PSE to flows in which multiple modes may play a role in the dynamics. These results are applicable to both incompressible and compressible flows.

The remainder of the paper is organized as follows. Section 2 contains a brief introduction to PSE, its well-known ill-posedness, and the three regularization techniques that can be used to stabilize the method. The main theoretical results of the paper are derived and analyzed in Sect. 3. Section 4 contains two example problems that are used to demonstrate and verify the theory. Finally, we summarize the contributions of the paper and discuss approaches that can be used in conjunction with or in place of PSE to eliminate these errors in Sect. 5.

2 Parabolized stability equations

2.1 Formulation

The mathematical formulation of PSE begins with the Navier–Stokes equations, which we represent compactly as

$$\mathscr{F}(q) = 0, \tag{1}$$

where $\boldsymbol{q}$ is a state vector of flow variables and $\mathscr{F}$ represents either the incompressible or compressible Navier–Stokes operator, which we will treat together whenever possible. The state vector is next decomposed into a steady base state $\bar{q}$ and fluctuations q' about it:

$$q(x, y, t) = \bar{q}(x, y) + q'(x, y, t). \tag{2}$$

Here, x is the slowly varying direction and y represents any number of orthogonal dimensions. The coordinates need not be Cartesian (PSE has been implemented for polar, cylindrical, and general curvilinear coordinates in additions to two- and three-dimensional Cartesian coordinates). The base state is usually chosen to be a (possibly approximate) laminar equilibrium or the mean of a turbulent flow. Inserting the decomposition into Eq. (1) and isolating the terms that are linear in q' yield an equation of the form

$$\mathscr{L}(\bar{q})\, q' = f\left(\bar{q}, q'\right), \tag{3}$$

where $\mathscr{L} = \left.\frac{\partial \mathscr{F}}{\partial q}\right|_{\bar{q}}$ is the linearized Navier–Stokes operator and f contains the remaining nonlinear terms. Assuming the flow to be statistically stationary, the fluctuation q' can be further decomposed into Fourier modes:

$$q'(x, y, t) = \sum_{\omega} \hat{q}_\omega(x, y)\, e^{-i\omega t}. \tag{4}$$

Substituting this into Eq. (3) and Fourier decomposing the nonlinear term lead to an equation of the form

$$\mathscr{L}_\omega \hat{q}_\omega = \hat{f}_\omega \tag{5}$$

for each ω, where $\mathscr{L}_\omega$ is the frequency domain linearized Navier–Stokes operator. The right-hand-side term contains the nonlinear contributions from all frequencies to the frequency ω. No approximation has been made to this point.

As discussed in Sect. 1, the fundamental assumption of the PSE method is that the streamwise behavior of the solution $\hat{q}_\omega$ can be decomposed into a rapidly varying wave-like component that is defined by a single complex wavenumber and a slowly varying modulation of this wave. This is embodied by the PSE ansatz:

$$\hat{q}_\omega(x, y) = \tilde{q}_\omega(x, y)\, e^{i \int \alpha_{0,\omega}(x) \mathrm{d}x}. \tag{6}$$

This ansatz is similar to that of classical linear stability theory, except that here both the shape function $\tilde{q}_\omega$ and wavenumber $\alpha_{0,\omega}$ are allowed to vary in x. It also bears resemblance to WKB and other multiple-scale expansions of $\hat{q}_\omega$, but PSE adopts a unique approach for computing the wavenumber and shape function. Since streamwise variation can be absorbed by either the shape function or the exponential term, an additional constraint must be imposed to uniquely define the solution and force the exponential term to absorb as much of the streamwise variation as possible, thus rendering the shape function slowly varying. A common choice that accomplishes this goal is to force the shape function to satisfy the condition [5]

$$\int_y \tilde{q}_\omega^* \frac{\partial \tilde{q}_\omega}{\partial x} \mathrm{d}y = 0, \tag{7}$$

where the asterisk superscript denotes the conjugate transpose.

Applying the PSE ansatz to Eq. (5), neglecting terms involving the second streamwise derivatives of the shape function (the effect of this step will be discussed in the next section), and solving for the first streamwise derivative yield an equation of the form

$$\frac{\partial \tilde{q}_\omega}{\partial x} = \tilde{\mathscr{M}}_\omega \tilde{q}_\omega + \hat{g}, \tag{8}$$

where $\hat{g}$ is the modified nonlinear term obtained after the preceding algebra. These are the nonlinear parabolized stability equations. Linear PSE is obtained by neglecting $\hat{g}$, which has the effect of decoupling each frequency from the rest. Our analysis will focus on linear PSE (so we set $\hat{g} = 0$ from here on out), but the linear errors we uncover are also relevant for nonlinear PSE, in which case errors at one frequency not only effect the linear evolution at that frequency, but also contaminate other frequencies through nonlinear interactions. Since linear PSE evolves each frequency independently, we drop all ω subscripts in what follows. In solving for the streamwise derivatives, we have assumed that the matrix pre-multiplying these terms is nonsingular, which is true when the mean streamwise velocity is nonzero and nonsonic everywhere. This assumption is convenient for simplifying our later analysis but is not strictly necessary—the same results can be obtained in the singular case by replacing the eigenvalues problems that appear throughout the ensuing analysis with appropriate generalized eigenvalue problems, as discussed by Towne and Colonius [44].

Finally, the defining feature of the PSE approach is the manner in which the equations are solved—via spatial marching. Specifically, Eq. (8) is solved as a spatial initial value problem in which an "initial" perturbation is specified at some streamwise position and propagated by integrating the equations in the slowly varying x direction. At each step in the march, the solution is iteratively adjusted to satisfy the constraint. The initial conditions for the shape function and wavenumber are usually chosen to be an eigenfunction–eigenvalue pair from a locally parallel linear stability analysis at the initial streamwise position and are therefore used to set the mode that PSE will attempt to track.

2.2 Instability and ill-posedness

It was noticed soon after the introduction of PSE that its spatial march is unstable if an explicit integrator, or an implicit integrator with a sufficiently small streamwise step size, is used [9]. It was soon after shown that the instability is caused by upstream-traveling modes of the local linearized Navier–Stokes equations that remain in the PSE operator, which make the equations formally ill-posed as a spatial initial value problem [18,25,26]. The mathematical nature of the linearized Navier–Stokes equations guarantees that upstream-traveling modes will appear in any flow with subsonic regions, even if second streamwise derivatives are neglected [24]. For well posedness, the downstream-traveling modes should be specified at the domain inlet and the upstream-traveling modes should be specified at the domain outlet. If instead the problem is solved as an initial value problem in space—by specifying all modes at the inlet and marching the solution downstream—the upstream-traveling modes will cause instability in the march. Specifically, decaying upstream-traveling modes are wrongly interpreted as growing downstream-traveling modes, leading to spurious exponential growth of the mode as it is integrated in the positive x-direction.

The precise identity of the offending modes depends on the flow. For example, the instability in compressible, external flows with subsonic far-field conditions is typical caused by continuous spectra that represent upstream-traveling acoustic waves, while the incompressible remnants of these branches cause instability in similar incompressible flows. In contrast, for flows that are supersonic except in limited regions, such as supersonic boundary layers, the instability is caused by discrete modes associated with the subsonic region near the wall [26].

Applying the PSE ansatz to the linearized Navier–Stokes equations and neglecting second streamwise derivatives of the shape function eliminate some of the upstream branches (particularly those related to viscous diffusion), but do not fundamentally alter the remaining modes. In particular, the PSE ansatz has the effect of simply shifting the remaining linearized Navier–Stokes spectrum such that the PSE wavenumber α_0 lies at the origin in the complex wavenumber plane. This is exactly true if the

$$\frac{1}{Re} \frac{\partial^2 \hat{q}}{\partial x^2} \tag{9}$$

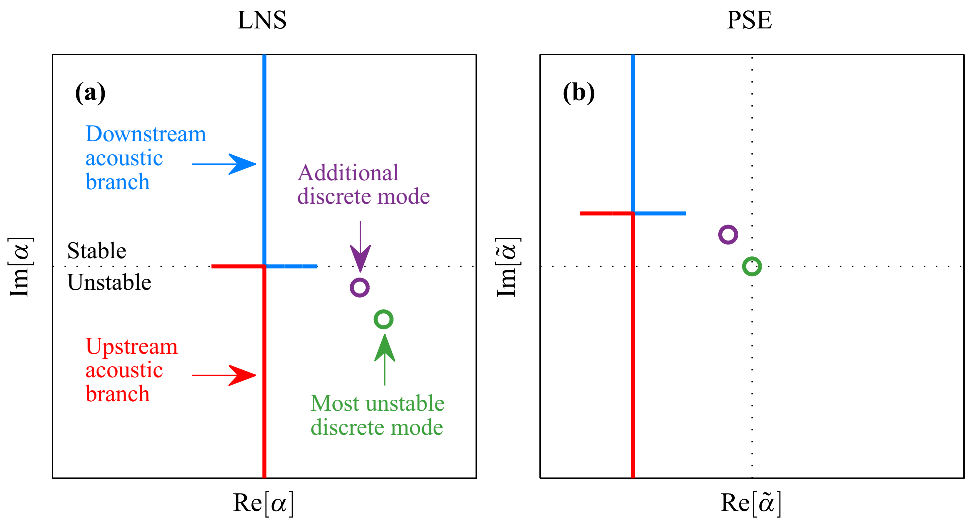

Fig. 1 An example of the spectra for **a** the linearized Navier–Stokes equations and **b** the parabolized stability equations. The LNS spectrum contains upstream and downstream acoustic branches and discrete convective modes. The PSE spectrum is identical, but shifted so that the most unstable mode lies at the origin. The remaining upstream acoustic branch makes spatial integration of the equations ill-posed

terms in the linearized Navier–Stokes equations are neglected (which is a slightly stronger assumption than already invoked by PSE, i.e., that $\partial^2\tilde{q}/\partial x^2$ is negligible) and is approximately true in general [26]. We will make this approximation to simplify the discussion and our later analysis. This simplification *reduces* the difference between the PSE and LNS operators, so our later error analysis is conservative; carrying the neglected terms through the analysis would result in additional differences between the downstream-traveling PSE and LNS modes in addition to those that will be identified by our simplified analysis.

Under this simplification, the linearized Navier–Stokes equations can be written

$$\frac{\partial \hat{q}}{\partial x} = \mathscr{M}\hat{q} \tag{10}$$

before applying the PSE ansatz [44], and the PSE operator $\tilde{\mathscr{M}}$ is related to the spatial LNS operator $\mathscr{M}$ as

$$\tilde{\mathscr{M}} = -i\alpha_0 I + \mathscr{M}, \tag{11}$$

where I is the identity matrix of appropriate dimension. From Eq. (11), it is clear that if $i\alpha$ is an eigenvalue of $\mathscr{M}$, then $i\tilde{\alpha} = i\alpha - i\alpha_0$ is an eigenvalue of $\tilde{\mathscr{M}}$. Furthermore, the eigenvectors associated with $i\alpha$ and $i\tilde{\alpha}$ are identical. Therefore, the modes of the PSE operator are the same as the modes of the spatial LNS operator, except that the PSE eigenvalues are shifted so that the PSE wavenumber α_0 lies at the origin in the $\tilde{\alpha}$-plane. Therefore, the ill-posedness of the LNS equations as a spatial initial value problem is inherited by the PSE operator, leading to instability in the spatial march.

To further illustrate these ideas and motivate the remainder of the paper, consider the hypothetical model spectrum shown in Fig. 1. This "cartoon spectrum" is not associated with any real flow, but it illustrates features that are typical of a compressible, external flow with a subsonic free stream, and it qualitatively contains the essential features that underpin the ill-posedness and instability of the PSE spatial march in general.

The two continuous branches represent upstream- and downstream-traveling free-stream acoustic waves and are given by the equation

$$\alpha_{\pm}(z) = \omega\,\frac{-M \pm \mu(z)}{1 - M^2}, \tag{12}$$

where M is the free-stream Mach number (which we assume for now to be less than one), $z \in [0, \infty]$ can be thought of as a transverse wavenumber, and the function $\mu(z)$ is given by

$$\mu(z) = \sqrt{1 - (1 - M^2)z^2}. \tag{13}$$

The part of each branch that lies along the imaginary axis represents acoustic waves that neutrally propagate away from their source in all directions, while the vertical parts represent evanescent acoustic waves that decay in the direction of propagation. Similar branches exist in incompressible subsonic flows, representing acoustic waves in the incompressible limit, but in that case all of the waves are evanescent . Therefore, the compressible acoustic branches considered here qualitatively contain the incompressible branches as a special case.

Our model spectrum additionally contains two downstream-traveling discrete modes. The mode with the more negative value of α_i represents the most convectively unstable mode of the flow (at the present streamwise location). A thorough discussion of the concept of convective instability can be found, for example, in Huerre and Monkewitz [21] and Schmid and Henningson [35]. The physical identity of the most unstable mode depends on the flow. For example, in free shear flows it might describe the Kelvin–Helmholtz instability while in wall-bounded flows it might describe a Tollmien–Schlichting wave. Finally, a second convectively unstable mode is included in our model spectrum. Not all flows contain a second unstable mode, but as discussed in Sect. 1 many flows of interest do have multiple unstable modes. We include this mode in our spectrum in order to study its treatment by PSE.

Assuming that we wish to track the spatial evolution of the most unstable discrete mode, applying the PSE ansatz to the model LNS spectrum results in the PSE spectrum shown in Fig. 1b. As already described, the PSE spectrum is identical to the LNS spectrum, but shifted by the PSE wavenumber. Since we wish to track the most unstable mode, the PSE wavenumber has been set to the value of the most unstable eigenvalue. If we now attempt to spatially integrate the PSE equations, the upstream acoustic branch (α_-) will cause instability in the march. Functionally, this is the case because the evanescent portion of the branch (which exists in both compressible and incompressible flows) takes on complex values with negative imaginary part, causing exponential growth of the mode as it is integrated in the positive x-direction. Therefore, additional regularization is required to achieve a stable spatial march.

2.3 Regularization methods

Several different regularization techniques have been proposed to stabilize the PSE march. The standard approach numerically damps the unstable upstream acoustic waves by using implicit Euler integration to advance Eq. (8) with a restriction on the *minimum* streamwise step size [25,26]. This is illustrated in Fig. 2 for our model spectrum. The gray region in each plot is the stability region of the implicit Euler integration, while the inner circle is the unstable region. The unstable region is centered at $\left(0, -\Delta x^{-1}\right)$ in the complex $\tilde{\alpha}$-plane, and its radius is equal to the inverse step size Δx^{-1}. If a sufficiently large step size is used, the upstream acoustic branch falls entirely within the region of stability, as shown in Fig. 2a. Therefore, the PSE equations can be stably integrated despite their ill-posedness. However, if the step size is made to be too small, part of the upstream branch enters the unstable region, as shown in Fig. 2b, and the streamwise march becomes unstable.

Therefore, there exists a minimum stable step size. Specifically, Δx must be large enough that no upstream-traveling modes reside within the unstable circle. Based on the geometry of the stability region, this requirement is formalized by the stability criterion

$$\Delta x > \Delta x_0 \tag{14}$$

with

$$\Delta x_0 = \max\left(-\frac{2\ \mathrm{Im}\left[\alpha_u - \alpha_0\right]}{\left|\alpha_u - \alpha_0\right|^2}\right), \tag{15}$$

where the maximum is taken over every upstream-traveling LNS mode α_u. When the mode that maximizes the expression is part of the upstream-traveling acoustic branch, as in our model spectrum, Eq. (15) becomes

$$\Delta x_0 = \frac{1}{\left|\mathrm{Re}\left[\alpha_0\right] + \dfrac{\omega M^2}{1 - M^2}\right|}. \tag{16}$$

Setting $M = 0$ recovers the more commonly quoted incompressible step-size restriction [25,26]

$$\Delta x_0 = \frac{1}{\mathrm{Re}\left[\alpha_0\right]}. \tag{17}$$

These same conditions hold if the PSE wavenumber is set so as to track the second convectively unstable discrete mode, as shown in Fig. 2d. A noteworthy feature of this plot is that the most unstable mode in this

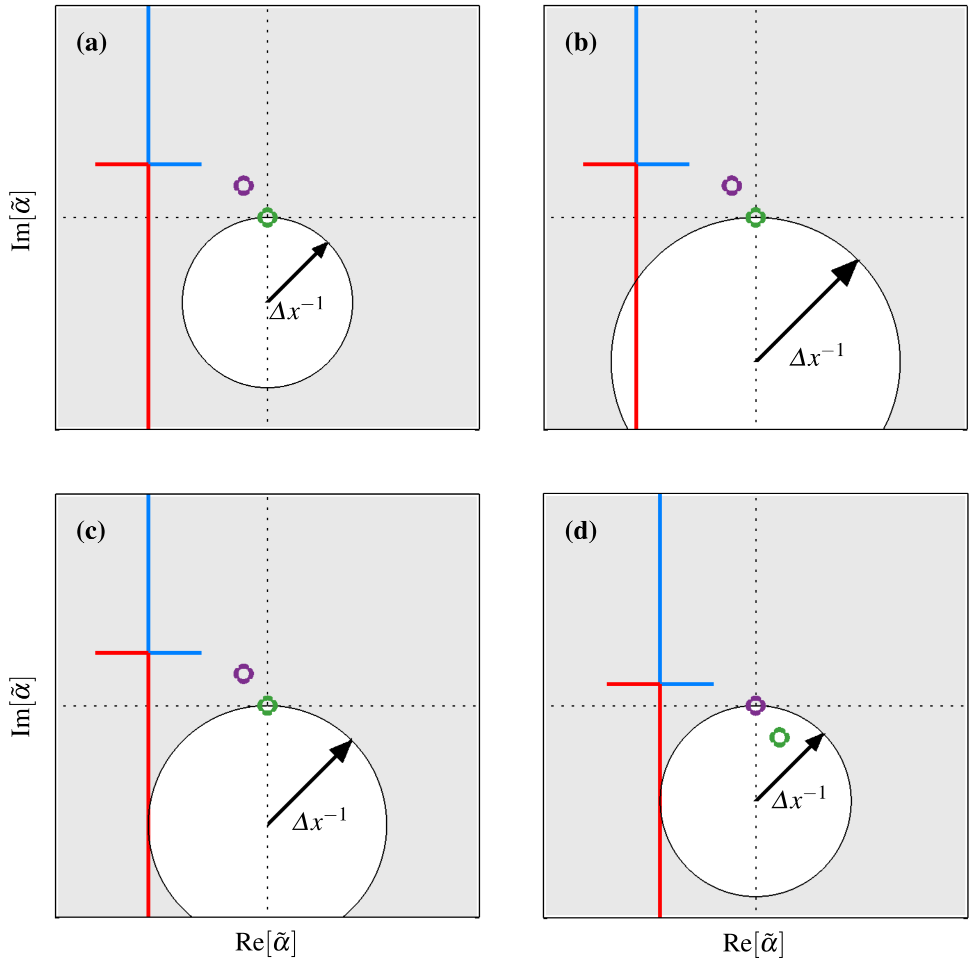

Fig. 2 Stabilization of the PSE march using the implicit Euler regularization technique. The shaded regions show the stability region of the implicit Euler integrator. **a** Using a sufficiently large step size numerically stabilizes the upstream acoustic branch (red line). **b** If the step size is reduced too much, the upstream acoustic branch again destabilizes the march. **c** Therefore, there exists a minimum step-size restriction for stability. **d** A similar step-size restriction exists if the PSE wavenumber is set to track other downstream modes (color figure online)

cases lies within the unstable region of the implicit Euler integrator. This is not necessarily a problem for the stability of the march, though, since this mode *should* grow more rapidly than the second mode that is being tracked. However, we will see in Sect. 3 that this situation can prevent the second mode from being accurately tracked.

Although this regularization technique successfully stabilizes the PSE march, the minimum step-size restriction makes it impossible to numerically converge the solution. This is clearly an undesirable trait for any method, and the step-size restriction is especially problematic for nonlinear versions of PSE in which implicitly discretized nonlinear terms must be iteratively converged at each step in the march. In this case, the large step size may cause the solution at one step to no longer be a sufficiently accurate guess for the solution at the next step, causing the iteration to fail. This issue led to the conception of two alternative regularization techniques meant to alleviate or eliminate the step-size restriction while still maintaining stability.

The first alternative regularization technique consists of neglecting the streamwise derivative of the pressure component of the shape function [9,18,25]. It should be noted that this is not the same as *setting* the streamwise derivative of the pressure to zero. This approximation has the effect of distorting the upstream acoustic branch and in particular moving it away from the usual location of unstable convective modes, thus reducing the minimum stable step size [25].

The second alternative method stabilizes the PSE march by explicitly adding a damping term to the PSE operator [1]. Specifically, Eq. (8) is replaced by the modified equation

$$\frac{\partial \tilde{q}}{\partial x} = \tilde{\mathscr{M}}\tilde{q} + s\tilde{\mathscr{M}}\frac{\partial \tilde{q}}{\partial x}, \tag{18}$$

where s is a parameter that controls the magnitude of the new damping term (and $\hat{g}$ has again been set to zero per our focus on linear PSE). The condition for the stability of implicit Euler integration of this equation can be shown to be [1]

$$\Delta x > \Delta x_0 - 2s, \tag{19}$$

where Δx_0 is given by Eq. (15) (or by Eq. (16) or (17) when applicable). As a result, the step-size restriction can be eliminated by setting $s = \Delta x_0/2$.

3 Analysis of the regularization methods

The three regularization techniques described in the previous section allow the PSE operator to be stably integrated in the slowly varying streamwise direction despite the inherent ill-posedness of the method. Our goal in this section is to analyze the impact of the regularization on the PSE solution and in particular on downstream-traveling LNS modes for which $\alpha \neq \alpha_0$. To do so, we will derive an expression for each regularization technique that describes the PSE propagation of each LNS mode and compare them with the correct LNS propagator.

We make two assumptions in these analyses. The first is that the term in Eq. (8) is negligible so that the relationship between $\mathscr{M}$ and $\tilde{\mathscr{M}}$ given in Eq. (11) holds. As previously discussed, the purpose of this simplification is to reduce the difference between the LNS and PSE operators and therefore makes our analyses conservative. Second, we assume that the slow streamwise variation of the LNS and PSE operators can be neglected over the distance of one step in the streamwise march. This assumption is justified by the slow streamwise variation of the underlying baseflow, is in line with the basic assumptions of PSE, and has also been made within previous mathematical analyses of PSE [1,18,19,25,26]. The purpose of this simplification is to enable mathematical analysis that will provide insight into the nature of the PSE method. The PSE errors identified under this approximation are expected to be illustrative of the kinds and magnitude of errors to be expected in nonparallel flows, but they are not necessarily a quantitative prediction of them. It is also implied throughout the analysis that the PSE wavenumber α_0 has been chosen such that the constraint given in Eq. (7) is satisfied. This is not an assumption, since it must be the case before the PSE solution can be advanced.

To provide a point of comparison, we begin by determining expressions for the correct propagation of upstream- and downstream-traveling LNS modes over an arbitrary interval $x_k < x < x_k + \Delta x$ as governed by the linearized Navier–Stokes equations. Under the locally parallel approximation described above, the solution in this interval can be written

$$\hat{q}_{\mathrm{LNS}}(x, y) = \sum_j \boldsymbol{v}_k^j(y)\,\hat{\psi}^j(x), \tag{20}$$

where each $(i\alpha_k^j, \boldsymbol{v}_k^j)$ is an eigenvalue–eigenvector pair of the LNS operator $\mathscr{M}$ at $x = x_k$ and $\hat{\psi}^j$ is a scalar expansion coefficient that defines the streamwise evolution of the amplitude and phase of the mode. The summation index j spans all of the eigenmodes admitted by the operator. Since Eq. (8) is linear and can be treated as spatially homogeneous over the Δx interval, each eigenmode can be treated independently. Therefore, we drop the j-superscript and k-subscript and consider an arbitrary mode with eigenvalue $i\alpha$, eigenvector v, and expansion coefficient $\hat{\psi}$. Within the locally parallel framework, only the expansion coefficient explicitly depends on the streamwise coordinate x. Inserting this local solution into Eq. (5) gives an evolution equation for the expansion coefficient:

$$\frac{\mathrm{d}\hat{\psi}}{\mathrm{d}x} = i\alpha\hat{\psi} \tag{21}$$

which can be integrated over the interval Δx to give

$$\hat{\psi}_{k+1} = e^{i\alpha\Delta x}\hat{\psi}_k. \tag{22}$$

Equation (22) defines the propagation of energy from ψ_k to ψ_{k+1} for each downstream-traveling mode and from ψ_{k+1} to ψ_k for each upstream-traveling mode.

3.1 Implicit Euler numerical damping

Our strategy for analyzing the PSE solution under the standard implicit Euler regularization technique is to derive an expression analogous to Eq. (22) that describes the evolution of the LNS modes within the PSE approximation.

Since the PSE operator $\tilde{\mathscr{M}}$ admits the same eigenfunctions as the LNS operator $\mathscr{M}$ (see Sect. 2.2), the PSE shape function in the interval $x_k < x < x_k + \Delta x$ can be written as a sum of LNS eigenfunctions, but with different coefficients since the PSE solution may differ from the LNS solution:

$$\tilde{q}\,(x, y) = \sum_j \boldsymbol{v}_k^j\,(y)\,\tilde{\psi}^j\,(x)\,. \tag{23}$$

Again, we drop the superscripts and subscripts and consider an arbitrary downstream-traveling mode with eigenvalue $i\alpha$, eigenvector v, and expansion coefficient $\tilde{\psi}$. As in Eq. (20), we have neglected the streamwise variation of v over the interval Δx using a locally parallel approximation in order to make the analysis tractable. Inserting this local solution into Eq. (8) gives the following evolution equation for the expansion coefficient:

$$\frac{\mathrm{d}\tilde{\psi}}{\mathrm{d}x} = (i\alpha - i\alpha_0)\,\tilde{\psi} = i\tilde{\alpha}\tilde{\psi}. \tag{24}$$

Here and in what follows, α_0 is understood to represent $\alpha_0\,(x_k)$.

For well posedness, this equation should be integrated from x_k to $x_k + \Delta x$ for downstream-traveling modes and from $x_k + \Delta x$ to x_k for upstream-traveling modes. Instead, PSE integrates all modes in the downstream direction, and stability is achieved, for the current regularization method, using an implicit Euler integrator:

$$\frac{\tilde{\psi}_{k+1} - \tilde{\psi}_k}{\Delta x} = i\tilde{\alpha}\tilde{\psi}_{k+1}, \tag{25}$$

which can be rearranged to give

$$\tilde{\psi}_{k+1} = \frac{1}{1 - i\tilde{\alpha}\,\Delta x}\tilde{\psi}_k. \tag{26}$$

The final PSE approximation of $\hat{q}$ is recovered from $\tilde{q}$ according to Eq. (6). Therefore, the PSE solution in the interval $x_k < x < x_k + \Delta x$ can be written in the form of Eq. (20) with each $\hat{\psi}$ replaced by a different expansion coefficient

$$\hat{\psi}^{\mathrm{PSE}}\,(x) = \tilde{\psi}^j\,(x)\,e^{i\alpha_0(x - x_k)}. \tag{27}$$

Equation (26) can therefore be written in terms of ψ^{PSE} as

$$\hat{\psi}_{k+1}^{\mathrm{PSE}} = \frac{1}{1 - i\tilde{\alpha}\,\Delta x}e^{i\alpha_0\Delta x}\hat{\psi}_k^{\mathrm{PSE}}. \tag{28}$$

To compare this result to the LNS solution, it is helpful to define a new eigenvalue α_e such that Eq. (28) can be written in a form equivalent to Eq. (22):

$$\hat{\psi}_{k+1}^{\mathrm{PSE}} = e^{i\alpha_e\Delta x}\hat{\psi}_k^{\mathrm{PSE}}. \tag{29}$$

Then α_e is determined by equating the propagators in Eqs. (28) and (29):

$$e^{i\alpha_e\Delta x} = \frac{1}{1 - i\tilde{\alpha}\,\Delta x}e^{i\alpha_0\Delta x}. \tag{30}$$

Solving for α_e gives

$$\alpha_e = \alpha_0 + \frac{i}{\Delta x}\log\left(1 - (i\alpha - i\alpha_0)\Delta x\right). \tag{31}$$

Noting the correspondence between Eqs. (22) and (29), we see that $i\alpha_e$ completely describes the PSE evolution of the LNS mode within the interval $x_k < x < x_k + \Delta x$ under standard implicit Euler regularization in the same way that $i\alpha$ governs the proper LNS evolution of the same modes. Therefore, we call $i\alpha_e$ the *equivalent PSE eigenvalue* for the LNS mode with eigenvalue $i\alpha$.

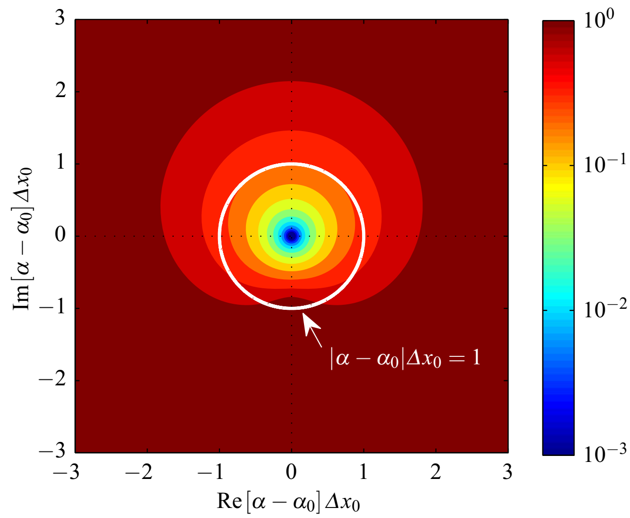

Fig. 3 Absolute value of the eigenvalue error ($|\alpha - \alpha_0|\Delta x_0$) caused by the implicit Euler PSE regularization. The error is small only for small values of the complex parameter $(\alpha - \alpha_0)\,\Delta x_0$, i.e., for LNS modes for which $\alpha \approx \alpha_0$

The difference between α_e and α quantifies the error in the PSE treatment of a mode with eigenvalue $i\alpha$. Precisely, we have

$$\delta\alpha_e \triangleq \alpha_e - \alpha = -(\alpha - \alpha_0) + \frac{i}{\Delta x}\log\left(1 - (i\alpha - i\alpha_0)\Delta x\right). \tag{32}$$

As $\Delta x \to 0$, the error $\delta\alpha_e$ goes to zero for all α, but this limit cannot be approached because of the PSE step-size restriction. At a finite Δx, the error in the PSE treatment of each mode depends only on its location in the complex plane relative to the primary mode α_0 and the step size. This result is completely generic and applies to any flow for which the two assumptions outlined at the beginning of Sect. 3 are valid, i.e., to weakly nonparallel flows. The error is minimized by setting the step size to its minimum stable value, so we set $\Delta x = \Delta x_0$ for the remainder of this section.

The magnitude of the error is depicted in Fig. 3 as a function of the position of an LNS eigenvalue α relative to the PSE wavenumber α_0. Both the axes and the error have been scaled by Δx_0. The form of the propagators in Eqs. (22) and (29) makes the step size a natural scaling for the error. (This will be further clarified shortly.) The contour levels are distributed logarithmically between 10^{-3} and 1 and are saturated beyond these values. The error is small for small values of $|\alpha - \alpha_0|\Delta x_0$. From Eq. (32), we see that the error is in fact zero for $\alpha = \alpha_0$, independent of step size. Moving away from $|\alpha - \alpha_0|\Delta x_0 = 0$, the error quickly becomes large; the radii of the regions where the error is less than 10^{-1} and 10^{-2} are approximately 0.46 and 0.14, respectively. We will see shortly that an error of 10^{-2} is already quite large. Therefore, the error $|\alpha_e - \alpha|\Delta x_0$ is small only for small values of $|\alpha - \alpha_0|\Delta x_0$.

The nature of the error can be better understood by considering its real and imaginary parts separately, each of which has a distinct meaning within the context of the equivalent PSE propagator from Eq. (29). First, consider the exact LNS propagator from Eq. (22). The amplitude and phase of this propagator represent the *change* in the amplitude and phase of the local LNS mode with eigenvalue $i\alpha$ over the step $\Delta x = \Delta x_0$ and are given by

$$|e^{i\alpha\Delta x_0}| = e^{-\mathrm{Im}[\alpha]\Delta x_0}, \tag{33a}$$

$$\angle\left(e^{i\alpha\Delta x_0}\right) = \mathrm{Re}\,[\alpha]\,\Delta x_0. \tag{33b}$$

The real and imaginary parts of $\alpha\Delta x$ therefore determine the change in phase and amplitude, respectively, of the mode over one step. Properly scaled, the phase can also be interpreted as the inverse of the local wavelength or phase speed of the mode described by the eigenvalue $i\alpha$.

Similarly, the amplitude and phase of the equivalent PSE propagator from Eq. (29) are

$$|e^{i\alpha_e\Delta x_0}| = e^{-\mathrm{Im}[\alpha_e]\Delta x_0}, \tag{34a}$$

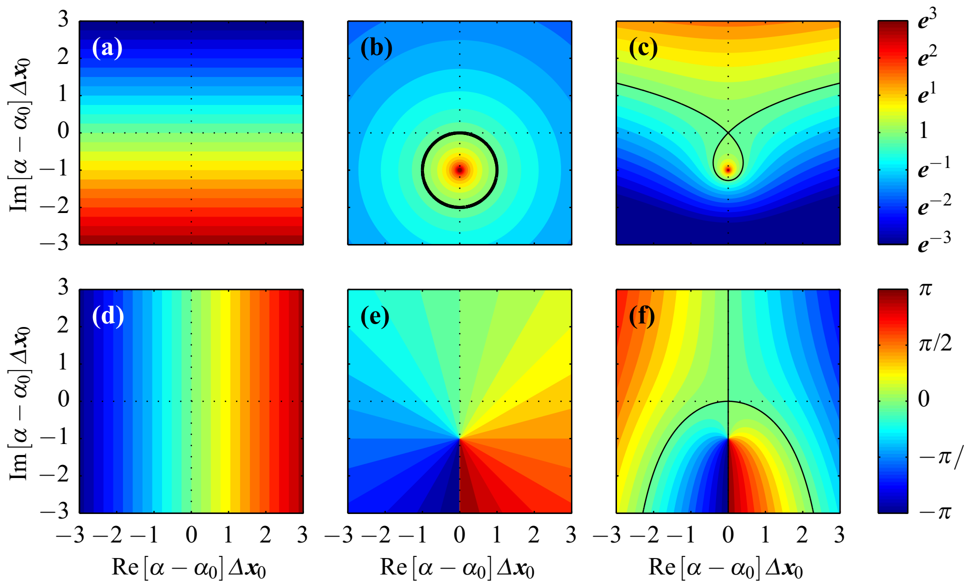

Fig. 4 Comparison between the LNS and PSE propagators for the implicit Euler regularization technique. Amplitude (first row) and phase (second row) of the relative LNS propagator $e^{i(\alpha-\alpha_0)\Delta x_0}$ (first column), relative PSE propagator $e^{i(\alpha_e-\alpha_0)\Delta x_0}$ (second column), and the error term $e^{i\delta\alpha_e\Delta x_0}$ (third column). The color bars pertain to all three sub-figures in their respective rows. The circle in **b** shows the boundary between growth and decay. The lines in **c** and **f** show the zero-error contours (color figure online)

$$\angle\left(e^{i\alpha_e\Delta x_0}\right) = \mathrm{Re}\,[\alpha_e]\,\Delta x_0, \tag{34b}$$

and are therefore determined by the imaginary and real parts of $\alpha_e\Delta x_0$, respectively. These quantities represent the change in amplitude and phase of an LNS eigenmode with eigenvalue $i\alpha$ over one step in the PSE march. The LNS and equivalent PSE propagators can be related using $\delta\alpha_e$. Specifically, the equivalent PSE propagator can be written as a product of the exact propagator and an error term:

$$e^{i\alpha_e\Delta x_0} = e^{i\alpha\Delta x_0}e^{i\delta\alpha_e\Delta x_0}. \tag{35}$$

Applying the standard rules of exponentiation to Eq. (35), the amplitudes and phases of the LNS and equivalent PSE propagators are related as

$$|e^{i\alpha_e\Delta x_0}| = |e^{i\alpha\Delta x_0}||e^{i\delta\alpha_e\Delta x_0}| = |e^{i\alpha\Delta x_0}|e^{-\,\mathrm{Im}[\delta\alpha_e]\Delta x_0}, \tag{36a}$$

$$\angle\left(e^{i\alpha_e\Delta x_0}\right) = \angle\left(e^{i\alpha\Delta x_0}\right) + \angle\left(e^{i\delta\alpha_e\Delta x_0}\right) = \angle\left(e^{i\alpha\Delta x_0}\right) + \mathrm{Re}\,[\delta\alpha_e]\,\Delta x_0. \tag{36b}$$

Therefore, the real and imaginary parts of the scaled error $\delta\alpha_e\Delta x_0$ represent an additive phase error and a multiplicative amplitude error incurred in one step of the PSE evolution of each LNS mode. The Δx_0 scaling of $\delta\alpha_e$ arises naturally in this analysis, which motivated our earlier use of this scaling for $|\delta\alpha_e|$.

The amplitude and phase of the LNS propagator, the equivalent PSE propagator, and the error term are visualized in Fig. 4. The two propagators are depicted in terms of their amplitude and phase *relative* to the primary mode being tracked. In other words, we show the amplitude and phase of $e^{i(\alpha-\alpha_0)\Delta x_0}$ and $e^{i(\alpha_e-\alpha_0)\Delta x_0}$ rather than $e^{i\alpha\Delta x_0}$ and $e^{i\alpha_e\Delta x}$. These relative propagators are advantageous because they are functions only of the difference $\alpha-\alpha_0$ rather than both α and α_0 independently. The error between these two relative propagators is still described by the error term $e^{i\delta\alpha_e\Delta x_0}$, as can be seen by factoring out $e^{i\alpha_0\Delta x_0}$ from both sides of Eq. (35).

The first row of Fig. 4 shows the amplitude of the two relative propagators and the error term as a function of the real and imaginary parts of $(\alpha-\alpha_0)\,\Delta x_0$. The contour levels are the same in all three plots and are logarithmically spaced. The amplitude of the relative LNS propagator is shown in Fig. 4a. By definition, it is a function only of the imaginary part of the shifted eigenvalue and therefore consists of horizontal lines in the complex $(\alpha-\alpha_0)\,\Delta x_0$-plane. A downstream-traveling mode whose eigenvalue has an imaginary part greater than or less than the imaginary part of α_0 is damped or amplified, respectively, relative to the primary mode described by the PSE wavenumber. The converse is true for upstream-traveling modes, as previously discussed in Sect. 2.2. The amplitude of the relative PSE propagator is shown in Fig. 4b. The black circle shows the location where the amplitude is one and exactly corresponds to the boundary of the stability region of the implicit Euler integration scheme, as depicted in Fig. 2. Assuming that the step size has been properly chosen, this ensures a stable march, since the amplitude is less than one everywhere outside of the circle. However, the substantial differences between the amplitudes of the LNS and equivalent PSE propagators make it clear that PSE will not properly evolve the amplitude of most LNS modes. This error is quantified by the amplitude of the error term $e^{i\delta\alpha_e \Delta x_0}$, which is shown in Fig. 4c. The black line shows the location where the amplitude of the error term is one, i.e., where the amplitude error is zero, and all other eigenvalues are either excessively damped or amplified.

Since these errors accumulate in each step of the PSE march, their values must be very low to accurately capture the amplitude of a given mode over the entirety of the march. For example, to achieve an accumulated amplitude error of less than 10% over only ten steps in the PSE march, the amplitude of the error term must on average fall in the range $e^{-0.01} < |e^{i\delta\alpha_e \Delta x}| < e^{0.01}$. It is clear from the figure that this is satisfied for a very limited region of the $(\alpha - \alpha_0)\, \Delta x$-plane. Therefore, most LNS modes will incur significant amplitude error in the form of either incorrect damping or amplification, depending on the value of their eigenvalue relative to the PSE wavenumber α_0.

We next consider the phase of the two relative propagators and the error term, which are shown as a function of the real and imaginary parts of $(\alpha - \alpha_0)\, \Delta x_0$ in the second row of Fig. 4. The contour levels are the same in all three plots and are linearly spaced between $-\pi$ and π. The phase of the relative LNS propagator is shown in Fig. 4d. By definition, the relative phase is equal to $\mathrm{Re}\,[\alpha - \alpha_0]\, \Delta x_0$ and thus manifests as evenly spaced vertical lines in the complex $(\alpha - \alpha_0)\, \Delta x$-plane. The phase of the relative PSE propagator is shown in Fig. 4e. The iso-contours take the form of rays emanating from the point $(0, -1)$, which is the branch point of the log function in Eq. (31). The phase jump from $-\pi$ to π across the ray along the negative imaginary axis corresponds to the associated branch cut. The obvious differences between the phases of the LNS and PSE propagators indicate that the PSE march will generate significant phase error for most LNS modes. This error is quantified by the phase of the error term, which is shown in Fig. 4f. These errors are incurred at every step in the PSE march and accumulate additively. For example, a mode with a 3 deg phase error at each steps is 30 deg out of phase after ten steps in the PSE march. This accumulated phase error can also be understood as an error in the wavelength or phase speed of the mode.

In summary, the PSE propagator associated with the implicit Euler regularization technique introduces both amplitude and phase errors relative to the LNS propagator. The size of these errors for a given mode depends on the location of its eigenvalue in the complex $(\alpha - \alpha_0)\, \Delta x_0$-plane. Both types of error are small only for eigenvalues that lie very near α_0. This is consistent with our previous discussion of the eigenvalue error $|\alpha_e - \alpha|$ shown in Fig. 3. As a result, only LNS modes for which $\alpha \approx \alpha_0$ can be accurately captured by PSE.

3.2 Pressure-gradient relaxation

Next, we turn our attention to the second regularization technique described in Sect. 2.3 in which the streamwise derivative of the pressure component of the PSE shape function is neglected. We will refer to this regularization approach as *pressure-gradient relaxation*. This approach reduces the step-size restriction but does not eliminate it. As a result, the modified equations must again be implicitly integrated, leading to the types of errors discussed in the previous section, but at a reduced level due to the smaller stable step size. While it is important to keep these errors in mind, the focus of this section is on characterizing the errors specifically caused by neglecting the pressure component of the streamwise derivative of the PSE shape function.

The approximation of neglecting the streamwise derivative of the pressure component of the PSE shape function can be represented by replacing Eq. (8) with a modified equation of the form

$$Z \frac{\mathrm{d}\tilde{q}}{\mathrm{d}x} = \tilde{M}\tilde{q}, \tag{37}$$

where Z has the effect of setting to zero the pressure component of the derivative term without modifying the other terms. For example, if pressure is explicitly chosen as one of the state variables, then Z is a diagonal matrix with a zero in the entry that multiplies the pressure component of the derivative and a one in each of the other (diagonal) entries.

To analyze the effect of this modification, we test whether an arbitrary downstream-traveling local LNS modes with eigenvalue $i\alpha$ and eigenvector v is also an approximate mode of Eq. (37). We know that this mode is also a mode of the PSE operator $\tilde{M}$ if α is replaced with the shifted eigenvalue $\tilde{\alpha}$:

$$\tilde{M}v = i\tilde{\alpha}v. \tag{38}$$

We next search for a perturbation to this mode that is a mode of Eq. (37):

$$\tilde{M}(v + \delta v) = i\left(\tilde{\alpha} + \delta\alpha_p\right) Z (v + \delta v). \tag{39}$$

The eigenvalue perturbation $\delta\alpha_p$ and the eigenvector perturbation δv represent the error introduced by neglecting the streamwise pressure derivative. Since the change between Eqs. (38) and (39) introduced by introducing Z is not small, the perturbations are not necessarily small and nonlinear products cannot be immediately neglected.

Before simplifying this expression, we search for conditions under which the LNS mode is an exact mode of the modified PSE Eq. (37), i.e., for which the eigenvalue and eigenvector perturbations are both zero. Setting $\delta\alpha_p$ and δv to zero in Eq. (39) and using Eq. (38) to eliminate $\tilde{M}$ lead to the condition

$$i\tilde{\alpha}(Zv - v) = 0. \tag{40}$$

An LNS mode with eigenvalue α and eigenvector v is also an exact mode of the modified PSE equations created by the pressure-gradient relaxation regularization technique only if it satisfies Eq. (40). There are two situations in which this condition is satisfied. First, it is satisfied if $\tilde{\alpha} = 0$, i.e., if $\alpha = \alpha_0$. Therefore, the primary LNS mode being tracked *is* a mode of the modified PSE given in Eq. (37). Since the numerical errors associated with the remaining step-size restriction are small for the primary mode, we conclude that it is accurately represented by PSE under pressure-gradient relaxation regularization. Second, condition (40) is satisfied if $Zv = v$. Since multiplication by the matrix Z has the effect of setting to zero the pressure, this relation is true only if the pressure component of the eigenvector v is identically zero. This is not the case for most physically relevant modes. Other than these two special cases, all other LNS modes are *not* modes of the regularized PSE. Therefore, the regularization causes errors in both the PSE eigenvalues and eigenvectors. This is fundamentally different from the first regularization technique which only caused errors in the effective representation of the eigenvalues.

To further simplify Eq. (37) in the case of nonzero error, we make use of the corresponding left-eigenvector u that satisfies the eigenvalue relation

$$u^*\tilde{M} = i\tilde{\alpha}u^*. \tag{41}$$

Left-multiplying Eq. (39) by u^* and using Eq. (41) to eliminate $\tilde{M}$ leave

$$i\tilde{\alpha}\, u^*(v + \delta v) = i\left(\tilde{\alpha} + \delta\alpha_p\right) u^* Z (v + \delta v) \tag{42}$$

and solving for the eigenvalue perturbation gives

$$\delta\alpha_p = \tilde{\alpha}\left(\frac{u^*(v + \delta v)}{u^* Z (v + \delta v)} - 1\right). \tag{43}$$

No assumptions have so far been made about the size of the perturbations.

The eigenvalue perturbation, which corresponds to the error in eigenvalue due to the PSE regularization, is small if one or both of the following conditions are met: $\tilde{\alpha} \approx 0$ or $u^*(v + \delta v) \approx u^* Z (v + \delta v)$. Using the definition of $\tilde{\alpha}$, the first condition can be written $\alpha \approx \alpha_0$. Therefore, modes that are very near the primary mode described by the PSE wavenumber are well represented by PSE. This is true regardless of the form of their eigenvector. The second condition requires that the pressure component of the perturbed eigenvector $v + \delta v$ is small compared to the other components. If we also insist that the eigenvector perturbation is small, which must be the case for the mode to be properly represented by PSE, this implies that the pressure component of the LNS eigenvector v must be small. This is a generalization of the earlier zero-error condition $Zv = v$ which required the pressure component to be zero. All other modes that do not satisfy one of these conditions will be poorly captured by PSE due to errors in both their eigenvalues and eigenvectors.

3.3 Explicit damping

Finally, we analyze the explicit damping regularization technique introduced by Andersson et al [1]. To do so, we follow an approach similar to that employed in Sect. 3.1 and derive an expression analogous to Eq. (21) that describes the PSE propagation of an arbitrary LNS mode. Beginning with the solution expansion from Eq. (23), we again consider a single arbitrary downstream-traveling LNS mode with eigenvalue $i\alpha$, eigenvector v, and expansion coefficient $\tilde{\psi}$. Inserting this local solution into Eq. (18) gives an evolution equation for the expansion coefficient:

$$\frac{\mathrm{d}\tilde{\psi}}{\mathrm{d}x} = \frac{i\tilde{\alpha}}{1 - s\, i\tilde{\alpha}}\tilde{\psi}. \tag{44}$$

Using Eq. (27) to eliminate $\tilde{\psi}^j$ in favor of $\hat{\psi}^{\mathrm{PSE}}$, Eq. (44) becomes

$$\frac{\mathrm{d}\hat{\psi}^{\mathrm{PSE}}}{\mathrm{d}x} = \left(i\alpha_0 + \frac{i\tilde{\alpha}}{1 - s\, i\tilde{\alpha}}\right)\hat{\psi}^{\mathrm{PSE}}. \tag{45}$$

If we set the damping parameter to $s = \Delta x_0/2$, then Eq. (45) can be integrated without a step-size restriction (see Sect. 2.3). As a result, it can be directly compared to the exact LNS evolution Eq. (21). Comparing Eqs. (21) and (45), we see that the LNS eigenvalue $i\alpha$ is replaced by a modified eigenvalue

$$i\alpha_s = i\alpha_0 + \frac{i\alpha - i\alpha_0}{1 - \frac{\Delta x_0}{2}\,(i\alpha - i\alpha_0)} \tag{46}$$

that describes the PSE evolution of the LNS mode. The difference between α_s and α quantifies the error in the PSE treatment of the mode:

$$\delta\alpha_s \triangleq \alpha_s - \alpha = -(\alpha - \alpha_0) + \frac{\alpha - \alpha_0}{1 - \frac{\Delta x_0}{2}\,(i\alpha - i\alpha_0)}. \tag{47}$$

Equation (47) shows that the error in the PSE representation of a mode with eigenvalue $i\alpha$ depends only on its location in the complex plane relative to the primary mode, i.e., $\alpha - \alpha_0$, and the nominal step-size restriction Δx^0. This was also the case for the implicit Euler regularization technique, while the error for the pressure-gradient relaxation technique depended on $\alpha - \alpha_0$ as well as the eigenvector of the mode. As was the case in both of these previous cases, the error is zero for the primary mode $\alpha = \alpha_0$.

Figure 5 shows the error as a function of the location of α in the complex plane relative to α_0. Both the axes and the error have been scaled by Δx_0. The contour levels are identical to those used in Fig. 3. Overall, Fig. 5 is extremely similar to Fig. 3 and the same conclusion holds— only LNS modes for which the distance between α and α_0 is small are accurately captured by PSE under the explicit damping regularization.

As before, the nature of the error can be elucidated by examining its real and imaginary parts separately. We again consider the real and imaginary parts of the relative PSE and LNS propagators and the error term, which are related as

$$e^{i(\alpha_s - \alpha_0)\Delta x_0} = e^{i(\alpha - \alpha_0)\Delta x_0} e^{i\delta\alpha_s \Delta x_0}. \tag{48}$$

To facilitate comparison with the results in Sect. 3.1, we have taken the step size to be $\Delta x = \Delta x_0$. This has no effect on the actual error, since α_s (and thus $\delta\alpha_s$) does not depend on the step size and the propagators in Eq. (48) are obtained via exact integration of the respective local evolution equations over the interval $x_k < x < x_k + \Delta x$. This choice is also convenient for plotting the results as it makes the scaled propagation error $\delta\alpha_s \Delta x_0$ a function of a single complex parameter $(\alpha - \alpha_0)\,\Delta x_0$ rather than of $\alpha - \alpha_0$, Δx_0, and Δx separately. Again, the error discussed here assumes exact integration of the regularized equations; the eventual numerical integration of the equations required in practice produces an additional error on top of that described here, but this is numerical error can be made arbitrarily small since no minimum step-size restriction exists in this case.

The amplitude and phase of the (relative) LNS propagator, the (relative) equivalent PSE propagator, and the error term are represented graphically in Fig. 6. The contour levels are identical to those used in Fig. 4 and are logarithmically spaced for the amplitude and linearly spaced for the phase. The amplitude and phase of the LNS propagator are shown in sub-figures (a) and (d), respectively, and are discussed in Sect. 3.1. The amplitude and phase of the PSE propagator are shown in sub-figures (b) and (e). The black circle in the amplitude plot shows the location where the amplitude is equal to one. It is centered at the point $(0, -1)$ in the $(\alpha - \alpha_0)\,\Delta x_0$

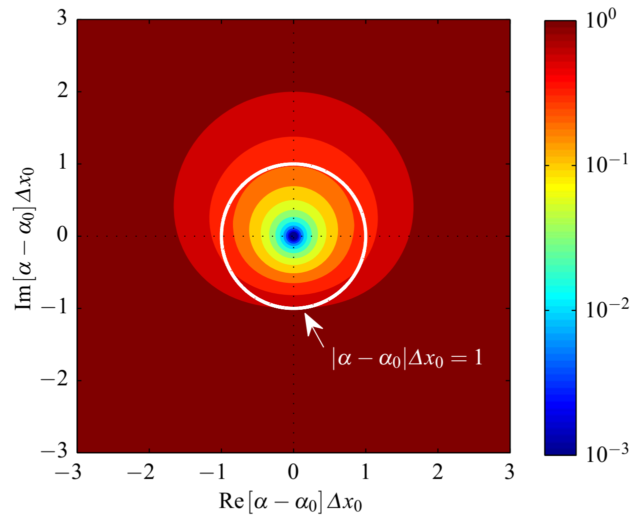

Fig. 5 Absolute value of the eigenvalue error ($|\alpha - \alpha_0|\Delta x_0$) caused by the explicit damping PSE regularization. The error is small only for small values of the complex parameter $(\alpha - \alpha_0)\,\Delta x_0$, i.e., for LNS modes for which $\alpha \approx \alpha_0$

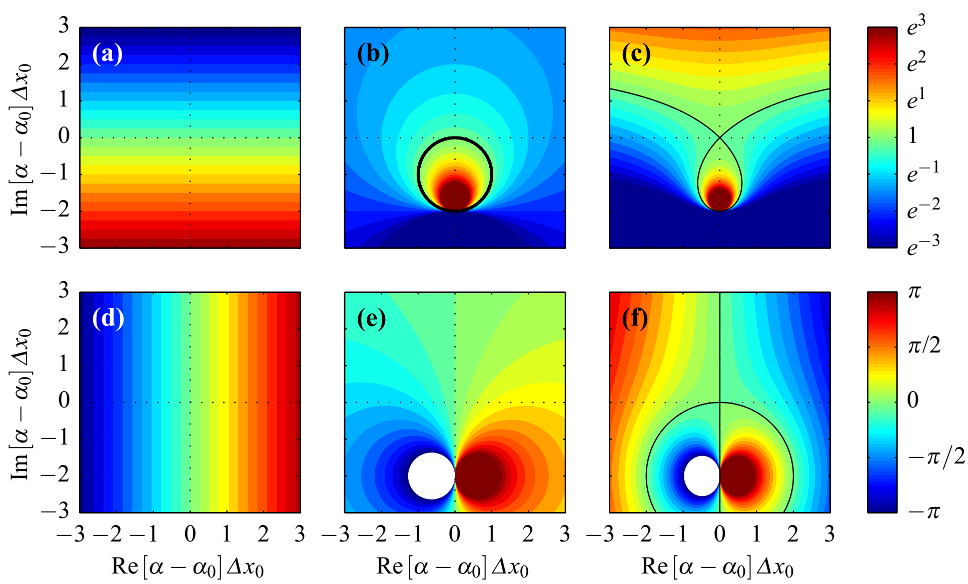

Fig. 6 Comparison between the LNS and PSE propagators for the explicit damping regularization technique. Amplitude (first row) and phase (second row) of the relative LNS propagator $e^{i(\alpha-\alpha_0)\Delta x_0}$ (first column), relative PSE propagator $e^{i(\alpha_e-\alpha_0)\Delta x_0}$ (second column), and the error term $e^{i\delta\alpha_e\Delta x_0}$ (third column). The color bars pertain to all three sub-figures in their respective rows and are the same as those in Fig. 4. The circle in **b** shows the boundary between growth and decay. The lines in **c** and **f** show the zero-error contours (color figure online)

plane and has a radius equal to one. All modes outside of the circle are damped. Assuming that Δx_0 has been properly chosen, this ensures a stable march.

The substantial differences between the LNS and equivalent PSE propagators are quantified by the error term $e^{\delta\alpha_s\Delta x_0}$. Its magnitude and phase are shown in Fig. 6c, f, respectively. Comparing these plots to Fig. 4c, f, we see that the errors produced by the explicit damping regularization are similar to those produced by the standard implicit Euler regularization. In particular, they are nearly identical for small values of $(\alpha - \alpha_0)\,\Delta x_0$. In fact, the first two terms in the Taylor series of $\delta\alpha_e\Delta x_0$ and $\delta\alpha_e\Delta x_0$ about $(\alpha - \alpha_0)\,\Delta x_0 = 0$ are identical. Notably, all of the conclusions made for the implicit Euler regularization hold as well for the explicit damping regularization. As before, both the amplitude and phase errors accumulate during the PSE march and must be very small at each step to achieve an accurate representation of a given mode.

3.4 Summary

Before considering some example problems, it may be helpful to summarize the key results of the three analyses presented in Sect. 3. Excluding the possible pathological cases discussed in Sect. 3.2, the central conclusion can be stated as follows: For all three regularization techniques, only LNS modes whose eigenvalues are near the eigenvalue of the primary mode being tracked can be accurately captured by PSE. For the implicit Euler and explicit damping regularization techniques, the error induced by the PSE regularization is confined entirely within the effective eigenvalues that govern the PSE evolution of each LNS mode; the eigenvectors are unaffected. On the other hand, the pressure-gradient relaxation regularization technique produces errors in both the eigenvalues and eigenvectors.

For flows containing multiple relevant modes, these results contrast the two usual interpretations of the PSE solution discussed in Sect. 1—that it represents either (i) a single mode or (ii) the true response of the initial perturbation. These scenarios would require high damping rates and low errors, respectively, for all modes other than the primary mode described by the PSE wavenumber. Figures 4 and 6 show that neither is true for the implicit Euler and explicit damping regularization methods, respectively. Similarly, our analysis of the pressure-gradient relaxation method shows that the error is not small away from the PSE wavenumber, and there is no reason to expect the damping to be universally large. Instead, our analysis suggests that the PSE solution will contain erroneous contributions from other LST modes for any of the three regularization techniques.

4 Examples

4.1 Free-stream acoustic waves

In this example, we examine the effect of PSE regularization on free-stream acoustic waves. Previous investigations have demonstrated that PSE is capable of capturing acoustic radiation in some cases but not others [10,11,23]. Our analysis here provides a rigorous explanation of these observations.

We describe the acoustic waves using the analytical eigenvalue expression provided in Eq. (12). These branches provide an excellent approximation of the real acoustic modes present in external flows such as boundary layers, mixing layers, wakes, and jets. We set $M = 0$, which corresponds to a quiescent free stream. Increasing the free-stream velocity tends to increase the distance (i.e., the difference in phase speeds) between convective and acoustic waves, so the zero-free-stream-velocity results can be interpreted as a lower bound on the error for flows with nonzero free-stream velocity. Thus, the $M = 0$ case represents a best-case scenario that minimizes the error incurred by the PSE approximation. To make the analysis as widely applicable as possible, we do not specify a form for the acoustic eigenvectors. While the far-field shape of the acoustic modes are essentially universal, their form in the near field can be different for different flows. This prevents us from analyzing the pressure-gradient relaxation regularization method but has no effect on the results for the other two methods, which depend only on the eigenvalues.

To compute the PSE approximation of the acoustic modes, we must also define the primary mode tracked by PSE by specifying a value for the PSE wavenumber α_0. To do so in a physically meaningful way, we choose values for the phase speed $c_p = \omega/\operatorname{Re}[\alpha_0]$ and the growth rate $g = -\operatorname{Im}[\alpha_0]/\omega$, which together define the frequency-scaled primary mode $\alpha_0/\omega = 1/c_p - ig$. The growth rate is defined such that the mode grows by a factor of e^{gc_p} over the distance Δx_0. We need not specify any specific form for the eigenvector of the primary mode, so it represents any mode of interest in any external flow.

To study the effect of regularization on the acoustic modes, we compute their PSE approximation for an array of values for c_p and g. In each case, Δx_0 is chosen according to Eq. (17). Results are shown in Figure 7 for $c_p = 2, 0.5, 0.2$ (from left to right) and $g = 0, 0.5, 1$ (from top to bottom), which together cover a physically relevant range of values. The axes have been scaled by ω, which make the results frequency independent. In each sub-figure, the circle shows the location of the primary mode α_0/ω. The solid lines show the exact downstream acoustic branch α_+, while the two broken lines are the corresponding PSE approximations α_e and α_s.

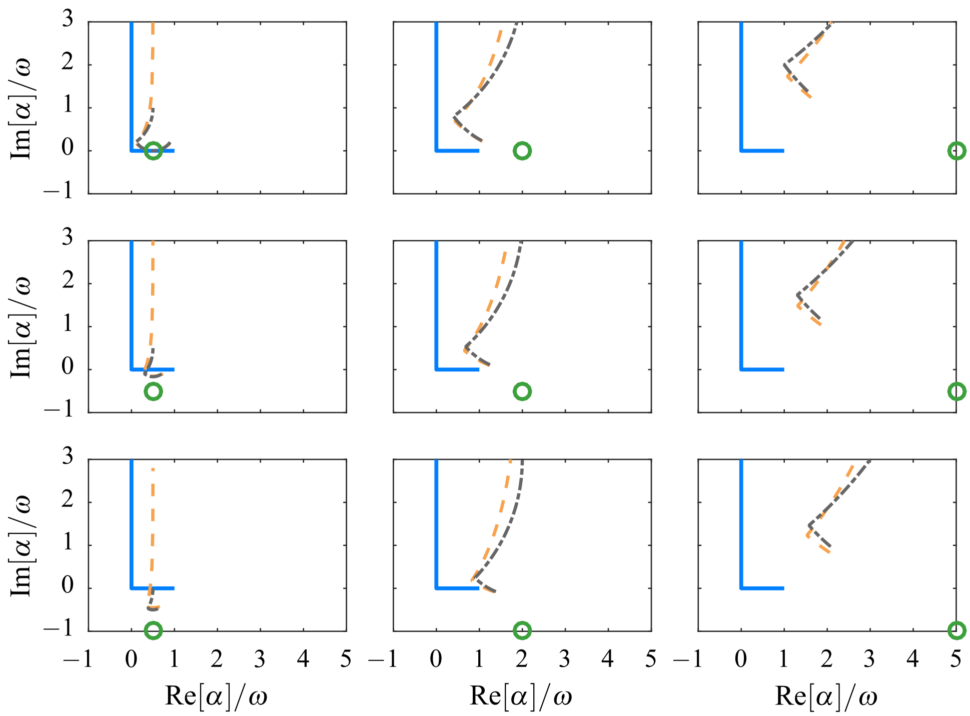

Fig. 7 PSE approximation of downstream acoustic waves: (blue line) exact acoustic branch; (spaced line) PSE approximation for the implicit Euler regularization technique; (spaced dotted line) PSE approximation for the explicit damping regularization technique; (circle) location of α_0, which correspond to the phase speeds $c_p = 2, 0.5, 0.2$ (from left to right) and the growth rates $g = 0, 0.5, 1$ (from top to bottom) (color figure online)

The horizontal part of the α_+ branch is particularly important as it represents propagative acoustic waves that do not decay as they travel downstream. In contrast, the vertical part of the branch represents evanescent acoustic waves that decay as they propagate. The propagative α_+ modes are mapped to the parts of the α_e and α_s branches that lie between the branch point (where the branch begins) and the clear kink that exists in each branch. It is clear that the equivalent PSE eigenvalues that represent the propagative acoustic modes are in general themselves not propagative. For a fixed growth rate, decreasing the phase speed (and thus increasing $\mathrm{Re}\left[\alpha_0\right]/\omega$) has the effect of increasing the damping rates and decreasing the phase speeds of the PSE-approximated acoustic modes. For a fixed phase speed, increasing the growth rate from zero has the effect of decreasing the damping (or increasing the growth rate) and again decreasing the phase speed of the PSE-approximated acoustic modes. Overall, when the phase speed and growth rate of the primary mode are low, the PSE regularization damps the propagative acoustic waves. In contrast, when the phase speed of the primary mode is high, the PSE regularization actually causes the propagative acoustic waves to grow.

Regions in the complex α_0/ω-plane that exhibit these two different behaviors for the implicit Euler and explicit damping regularization methods are shown in Fig. 8. Specifically, the contour levels show the minimum value of $\mathrm{Im}\left[\alpha_{e,s}\right]/\omega$ for the propagative part of each PSE-approximated downstream acoustic branch. All acoustic waves are damped for α_0/ω values in regions where this value is positive, while modes on at least part of the propagative branch are growing when it is negative. The solid line shows the boundary between the two regions.

In boundary-layer flows, the real part of α_0 is typically an order of magnitude larger than the imaginary part [14,25]. The wedge-shaped region between the two broken lines satisfies this condition. Within this region, both PSE regularization methods always have the effect of damping the downstream propagative acoustic modes when the phase speed of the primary mode is subsonic ($\alpha_0/\omega > 1$). On the other hand, when the phase speed is supersonic ($\alpha_0/\omega < 1$), the growth rate of at least part of the propagative part of the acoustic branch is positive, albeit small.

In free shear flows, sound is produced in part by hydrodynamic structures called wavepackets that are created by modes that grow and then decay [22]. In particular, sound is emitted from the region where these structures reach their peak amplitude (where $\mathrm{Im}\left[\alpha_0\right] = 0$) and transmitted thereafter as the wavepacket decays

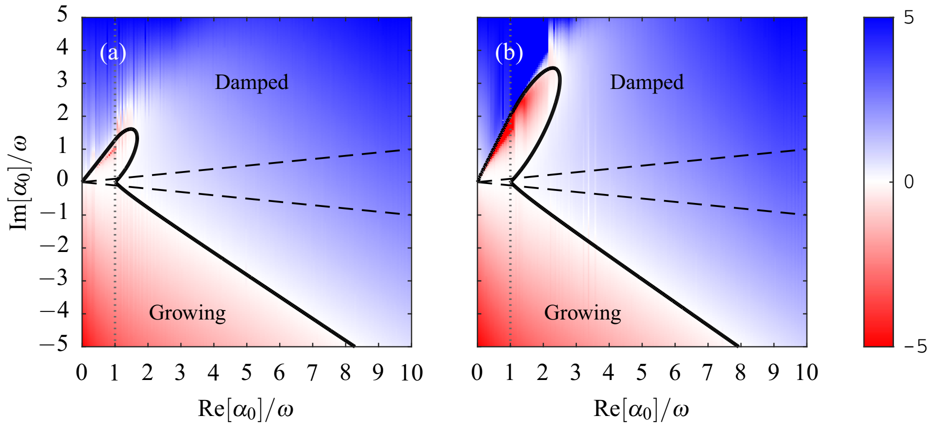

Fig. 8 Minimum value of **a** Im $[\alpha_e]/\omega$ and **b** Im $[\alpha_s]/\omega$ in the respective PSE approximations of the propagative part of the downstream acoustic branch as a function of the PSE wavenumber. All acoustic waves are damped for positive values, while modes on at least part of the propagative branch are growing when it is negative. The solid line shows the boundary between the two regions. The wedge-shaped region between the two dashed lines shows the region of α_0/ω space typical of boundary-layer flows. The vertical dotted line separates regions with supersonic (left) and subsonic (right) phase velocities

(where Im $[\alpha_0] > 0$). As a result, the situation where Im $[\alpha_0]/\omega \geq 0$ is most relevant for understanding the PSE treatment of acoustic waves in these flows. For small damping rates, both PSE regularization methods have the effect of damping acoustic waves when the phase speed of the primary mode is subsonic and amplifying them when the phase speed is supersonic. If the damping rate of the primary mode becomes large, the reverse situation is possible, but acoustic waves are always damped by PSE for phase speeds below 0.6 and 0.4 for the implicit Euler and explicit damping regularization techniques, respectively. This boundary is set by the maximum real part of the small unstable region in the upper half plane in Fig. 8. It is interesting that the PSE regularizations, which are designed to damp the upstream acoustic modes, can actually cause some or all of the downstream acoustic modes to grow in some cases.

These results provide an explanation of the observation made by several previous investigators that PSE provides a reasonable approximation of the acoustic radiation emitted from mildly supersonic flows but not from subsonic flows. For example, Cheung and Lele [10,11] found that while PSE accurately captured near-field Kelvin–Helmholtz instability waves in both supersonic and subsonic mixing layers, the associated acoustic radiation was reasonably captured only for the supersonic case and vastly under-predicted (by as much as five orders of magnitude) in the subsonic case. A similarly large under-prediction was reported by Towne [41] for a different subsonic mixing layer. Figures 7 and 8 provide an explanation of these observations in terms of the phase speeds of the Kelvin–Helmholtz instability waves that constitute the primary mode in these flows. The Kelvin–Helmholtz waves in the supersonic mixing layers considered in these investigations have phase speeds of between 1.8 and 2 [10]. Therefore, the error in the PSE representation of the acoustic modes is small and in particular the imaginary parts of the PSE eigenvalues are nearly zero, as they should be. The error that does exist in the imaginary part is likely to take the form of a small positive growth rate. Therefore, the far-field acoustic radiation in these mixing layers should be accurately captured by PSE, but slightly over-predicted. This is exactly what is observed in Figure 8(c) of Cheung and Lele [11] and numerous figures in Cheung and Lele [10]. The Kelvin–Helmholtz waves in the subsonic mixing layers considered in these investigations have phase speeds of less than 0.4 [10]. As a result, the PSE regularization generates significant error in the representation of the acoustic modes and in particular damps them significantly. Therefore, the far-field acoustic radiation should be severely under-predicted by PSE, as has been observed.

In addition to studying the propagative acoustic modes, it is of interest to scrutinize the PSE treatment of the part of the α_+ acoustic branch that has very large imaginary values, which describes evanescent acoustic mode that are highly damped. Figure 7 shows that the α_e approximations of the α_+ acoustic branch also goes to infinity for all of the selected c_p and g values, and this conclusion can be confirmed in general by computing the limit of Eq. (31). On the other hand, the α_s approximations of the α_+ acoustic branch remain contained within the relatively tight axes of the figure for $c_p = 2$ and all three values of g. Taking the limit of Eq. (46) as the imaginary part of α goes to infinity confirms that α_s asymptotes to a finite value for high damping rates.

In fact, this is a special case of a more general result:

$$\lim_{|\alpha|\to\infty} \alpha_e = \alpha_0 + \frac{2i}{\Delta x_0}. \tag{49}$$

If Δx_0 is chosen according to Eq. (17), the right-hand side of the limit can be written as $\alpha_0 + 2i\,\mathrm{Re}\,[\alpha_0]$. This result holds for any α, not just the acoustic branch. This shows that all LNS modes that are slow and/or highly damped are all mapped to the same equivalent PSE eigenvalue with real part equal to the real part of the primary mode and imaginary part equal to $\mathrm{Im}\,[\alpha_0] + 2\,\mathrm{Re}\,[\alpha_0]$. The damping rate of this PSE eigenvalue is therefore significantly underestimated and can even be negative when $\mathrm{Im}\,[\alpha_0] < -2\,\mathrm{Re}\,[\alpha_0]$. As a result, it is possible for waves that should be quickly damped to persist (or even grow) within the PSE solution when the equations are regularized using the explicit damping method.

4.2 Single-stream jet

Next, we consider the acoustic radiation emitted by a round jet, with the goal of verifying the trends observed in the previous section. The flow consists of a single stream of fluid with Mach number $M_a = U_j/c_\infty$ ejected from a nozzle of diameter D into ambient fluid at rest. The Reynolds number is $Re = U_j D/\nu_\infty = 3 \times 10^4$. An analytical expression is used to approximate the mean flow about which the Navier–Stokes equations are linearized. Following Crighton and Gaster [12], the mean streamwise velocity is given by the expression

$$\bar{u}_x = \frac{U_j}{2}\left\{1 + \tanh\left[\frac{D}{8\theta}\left(\frac{D}{2r} - \frac{2r}{D}\right)\right]\right\} \tag{50}$$

with a linearly increasing momentum thickness

$$\theta = \frac{3}{100}\left(x + \frac{2}{3}D\right), \tag{51}$$

the mean radial and azimuthal velocities are set to zero, and the mean density and pressure are set to constant values equal to their ambient values. Details of the linearized equations and their discretization can be found in Towne and Colonius [43].

The dominant instability mode of this flow is related to the Kelvin–Helmholtz instability of the shear layer between the jet and the ambient fluid. The phase speed of the Kelvin–Helmholtz mode increases with increasing Mach number [3], which allows us to vary the value of the key parameter $\mathrm{Re}\,[\alpha_0]/\omega$ by adjusting the Mach number. Accordingly, the results from Sect. 4.1 predict that PSE will damp the acoustic waves emitted by the jet more severely for lower Mach numbers.

To verify this prediction, we compare the LNS and PSE propagation of the Kelvin–Helmholtz mode and its emitted acoustic radiation for a range of Mach numbers. We consider axisymmetric perturbations at two different frequencies, $St = \omega D/(2\pi U_j) = 0.1$ and 0.3. For each case, the local Kelvin–Helmholtz mode at the jet inlet is provided as a boundary condition for a global LNS calculation and as the initial condition for a PSE calculation. The PSE march is regularized using the explicit Euler method, and each streamwise step is taken with the minimum stable step size.

The key results are summarized in Fig. 9. Here, we plot the ratio of the squared pressure amplitude computed via PSE and LNS at the location within the acoustic field where the LNS solution is largest, i.e., the location of maximum acoustic radiation. If the PSE solution were to faithful capture the acoustic field, this ratio would be equal to one; this value is indicated by the dashed line in the figure. Instead, we observe that the PSE solution under-predicts the acoustic radiation and that the under-prediction is increasingly severe with decreasing Mach number, as predicted by the theory. The error is smaller for the higher frequency at supersonic Mach numbers, consistent with the results of Sinha et al [37], but the magnitude of the error is still around 50%.

4.3 Dual-stream jet

Finally, we consider the example of a dual-stream jet, which serves as a demonstration of the detrimental impact of PSE regularization on a flow with multiple relevant instability modes. The flow consists of two coaxial streams: an inner stream with an initial diameter D and Mach number $M_1 = U_1/c_\infty = 1.26$ and an

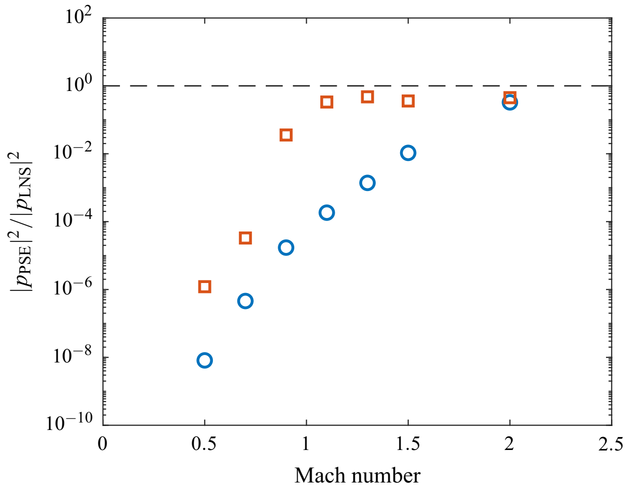

Fig. 9 Ratio of the pressure amplitude computed by PSE and LNS for a single-stream jet at the location of maximum acoustic radiation as a function of Mach number for two frequencies: (circle) $St = 0.1$ and (square) $St = 0.3$. Values less than one (dashed line) indicate that PSE has damped the acoustic radiation. The damping is more severe for lower Mach numbers, consistent with the theory developed in §4.1

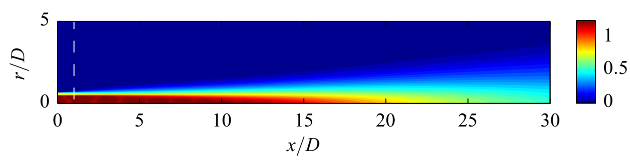

Fig. 10 Mean streamwise velocity of the compressible dual-stream jet. The dashed white line shows the streamwise location at which the LNS, PSE, and OWNS calculations are initiated

outer stream with initial diameter $1.33D$ and Mach number $M_2 = 0.8$. The jet is isothermal and the Reynolds number of the jet based on the inner jet velocity and diameter is $Re = U_1 D/\nu_\infty = 2.6 \times 10^6$.

The LNS and PSE operators for this flow were obtained by linearizing the compressible Navier–Stokes equations in cylindrical coordinated about the mean flow, which was computed from large-eddy simulation data computed by Brès et al. [8]. Information about the numerical method can be found in Brès et al. [7]. The mean streamwise velocity is shown in Fig. 10. Again, details of the linearized equations and their discretization can be found in Towne and Colonius [43]. Following Schmidt et al [36], we use a lower effective Reynolds number of 10^5 in the linear equations to mimic the effect of an unknown turbulent viscosity, but this ad hoc approximation has no bearing on the comparisons we make in what follows.

The dual-stream jet contains several relevant instability modes. As an example, a portion of the local LNS spectrum at $x/D = 1$ is shown in Fig. 11a for the frequency $St = \omega D/(2\pi U_1) = 0.3$. First, there are two discrete unstable downstream-traveling modes. These two modes are related to the Kelvin–Helmholtz instability of the two shears layers that form between the inner and outer streams and the outer and ambient free streams, respectively. This can be confirmed by calculating their phase speeds, which match those expected for the two shear layers, or by examining their eigenfunctions. The streamwise velocity components of the two unstable discrete modes are plotted along with the local mean streamwise velocity in Fig. 11a. Each mode clearly peaks at the radial r/D location of one of the shear layers. Additionally, the jet supports a series of neutrally stable discrete modes, which appear in Fig. 11a along the dashed line at $\mathrm{Im}[\alpha] = 0$. These represent a family of acoustic waves that are trapped within the inner potential core of the jet, which were identified by Tam and Hu [39] and recently investigated by Towne et al [45]. Finally, the jet supports downstream- and upstream-traveling free-stream acoustics waves, which appear in Fig. 11a as mostly vertical branches that asymptote toward $\mathrm{Re}[\alpha] = 0$ for $\mathrm{Im}[\alpha] \to \pm\infty$, respectively. Additional modes that are not important for the ensuing discussion, including stable convective modes and stable spurious modes that inevitably arise due to the dispersive nature of the finite-difference discretization used to approximate radial derivatives, are shown in the figure as light gray circles.

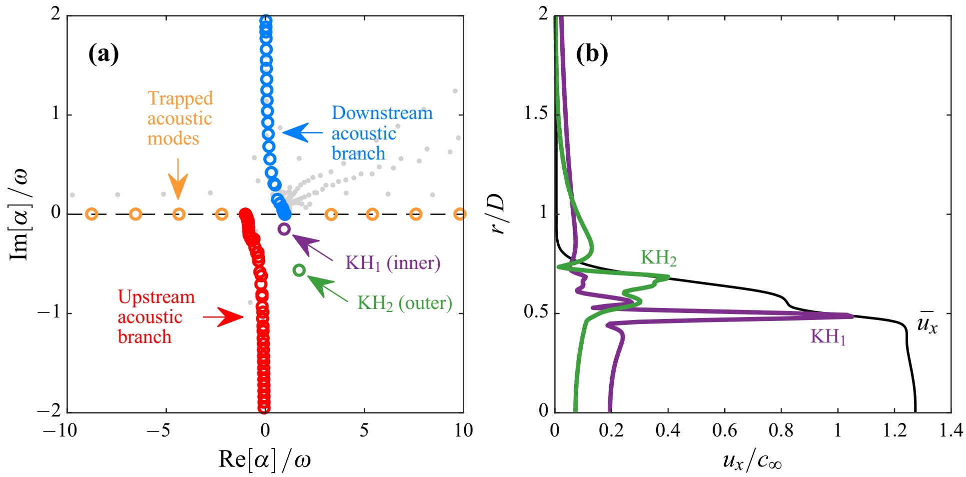

Fig. 11 Local eigenmodes of the dual-stream jet at $x/D = 1$. **a** Local LNS eigenvalues; **b** streamwise velocity component of the two Kelvin–Helmholtz modes superposed with the mean streamwise velocity. The amplitudes of the eigenvectors are arbitrary

This rich pool of modes supported by the dual-stream jet provides an opportunity to demonstrate the difficulty of applying PSE to flows with multiple relevant eigenmodes. We begin by comparing the LNS and PSE propagation of the inner Kelvin–Helmholtz mode. To do so, we provide the local inner Kelvin–Helmholtz mode at $x/D = 1$ as a boundary condition for a global LNS calculation and as the initial condition for a PSE calculation (as well as a one-way Navier Stokes calculation, which will be discussed later). The PSE march is regularized using the explicit Euler method, and each streamwise step is taken with the minimum stable step size.

The results are shown in Fig. 12. The two rows show the same data plotted using different contour levels chosen to highlight the results in the jet near field and acoustic field, respectively. In both the LNS and PSE solutions, the inner Kelvin–Helmholtz mode grows and then decays in the streamwise direction, leading to a wavepacket structure in the jet near field. PSE provides an excellent approximation of this wavepacket. In addition to the near-field wavepacket, the LNS solution also exhibits a strong beam of acoustic radiation that is admitted from the wavepacket near its location of peak amplitude. The PSE solution also contains this acoustic beam, but its amplitude decays more rapidly away from its source. This behavior is predicted by the analysis in Sect. 4.1. Even though the inner stream of the jet is supersonic, the phase speed of the inner Kelvin–Helmholtz mode is subsonic, with a value of about 0.7 near the location of peak amplitude. Thus, according to the analysis in Sect. 4.1, the acoustic LNS modes will be damped at each step in PSE march, leading to a decrease in amplitude with increasing x.

Next, we repeat the same exercise with the outer Kelvin–Helmholtz wave at $x/D = 1$ specified as the boundary condition and initial condition for the LNS and PSE calculations, respectively. Results are shown in Fig. 13. The LNS solution contains a short wavepacket generated by the outer Kelvin–Helmholtz mode, extending to about $x/D = 4$. Beyond this point, the solution is dominated by short-wavelength disturbances caused by the trapped acoustic waves. The PSE solution contains an accurate approximation of the initial Kelvin–Helmholtz wavepacket but completely misses the trapped acoustic waves. Additionally, the flooded contour levels in the second row of Fig. 13 show that the PSE solution contains a second wavepacket in the region $5 < x/D < 10$. This wavepacket is caused by the *inner* Kelvin–Helmholtz mode, which was excited by energy that leaked from the outer mode. This is consistent with the observations made by Sinha et al [38] for a different dual-stream jet.

In summary, we have demonstrated in this example that PSE fails to achieve either of the desired outcomes discussed in the introduction. On the one hand, it does not deliver a solution that consists of a single weakly nonparallel mode; the PSE solution contains acoustic waves and inner Kelvin–Helmholtz waves when the initial condition was set to be the inner and outer Kelvin–Helmholtz modes, respectively. On the other hand, PSE does not capture the complete downstream response to the initial condition; free-stream acoustic waves and trapped acoustic waves that were observed in the full LNS solution were damped by PSE in the two cases.

We stress that these issues are caused by the regularization required to stabilize the ill-posed PSE march, and there is no apparent way to fix these errors in the PSE framework. On the other hand, the one-way spatial

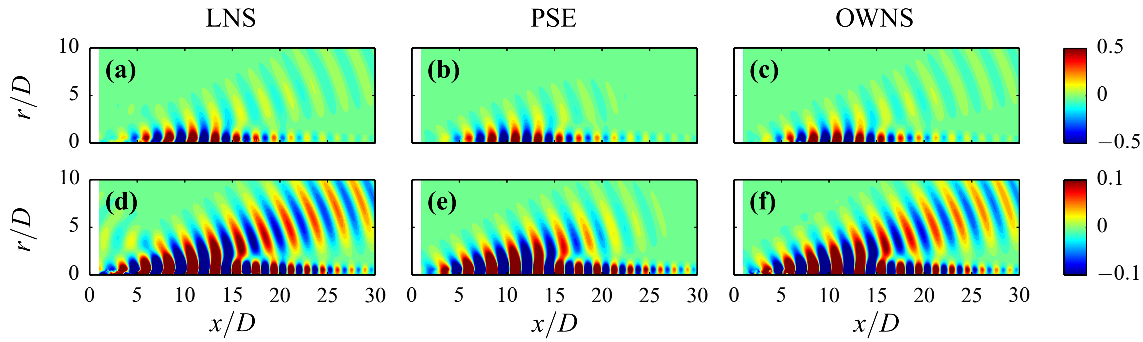

Fig. 12 Flow response using the inner Kelvin–Helmholtz mode (KH_1) as the initial condition at $x/D = 1$. Contours of the real part of the pressure perturbation: **a** LNS; **b** PSE; **c** OWNS. The same data are shown in both rows, with contour levels selected to highlight the near field and acoustic field in the top and bottom rows, respectively

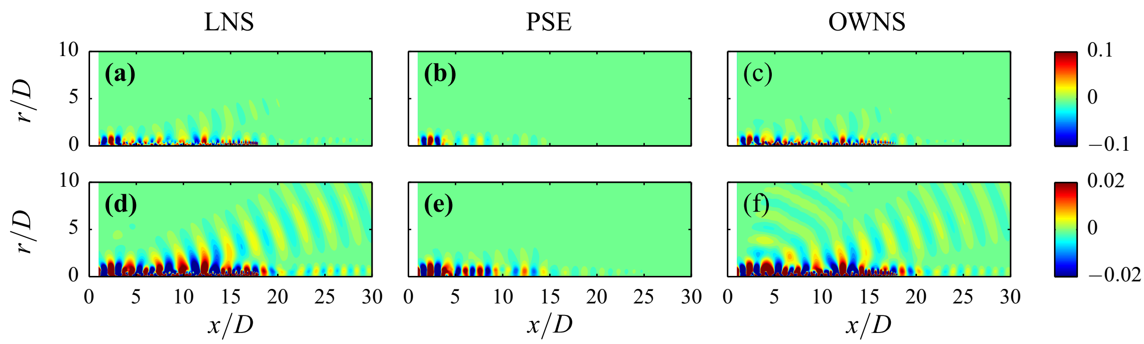

Fig. 13 Flow response using the outer Kelvin–Helmholtz mode (KH_2) as the initial condition at $x/D = 1$. Contours of the real part of the pressure perturbation: **a** LNS; **b** PSE; **c** OWNS. The same data are shown in both rows with different contour levels

integration method introduced by Towne and Colonius [44] overcomes these issues by constructing well-posed spatial evolution equations that do not require detrimental PSE-like regularization. For example, the one-way Navier–Stokes (OWNS) solutions for the inner and outer Kelvin–Helmholtz initial conditions are shown in the right-most columns of Figs. 12 and 13, respectively (see Towne and Colonius [43] for details on the application of this method to jets). In both cases, the OWNS solution matches well with the global LNS solution, indicating that, unlike PSE, OWNS has properly captured the complete downstream response of the initial perturbation. While not the topic of this paper, recent applications of OWNS to boundary layers Rigas et al [31] and for computing optimal (forced) disturbances Rigas et al [32] provide a promising alternative to PSE for flows involving multiple unstable modes and acoustic radiation. It must be noted, however, that the additional fidelity of OWNS comes with a corresponding increase in computational complexity and operation count.

5 Conclusions

In this paper, we have performed a spectral analysis of the PSE operator to elucidate the behavior of LNS modes whose wavenumber and growth rate differ from the primary disturbance begin tracked. The implicit assumption made in many applications of PSE is that these other modes are either quickly damped so that the solution can be regarded as an approximation of a single global mode or accurately propagated so that the solution can be interpreted as the complete response to the initial perturbation. Our results show that neither of these behaviors are generally true. These errors arise not because of the PSE ansatz given in Eq. (6), but rather due to regularization techniques that must be applied to stabilize the downstream march due its inherent ill-posedness. For the implicit Euler and explicit damping regularizations, the error manifests exclusively in the effective eigenvalues that govern the PSE approximation of the evolution of each mode, leading to incorrect wavelengths and growth rates. The pressure-gradient relaxation technique leads to errors in both the eigenvalues and eigenvectors.

In flows dominated by a single unstable mode, these errors will have little impact on the accuracy of PSE, as suggested by its success in these cases. On the other hand, the errors can be significant for applications in which multiple modes are relevant to the flow dynamics. Examples include flows involving acoustic waves, multiple unstable modes, or transient growth. The effect of PSE on acoustic waves is considered in Sect. 4.1. We showed that PSE can lead to either excessive damping or growth of acoustic waves, depending on the wavelength and growth rate of the primary mode being tracked. These results explain previous observations made by Cheung and Lele [11], Towne and Colonius [42], and others.

The detrimental effects of the PSE regularization predicted by the theory developed in this paper were demonstrated for the example of compressible dual-stream jet. The local LNS operator for this flow supports several different types of modes, including two unstable Kelvin–Helmholtz modes associated with the two shear layers between the two streams of the surrounding ambient flow. Using these two Kelvin–Helmholtz modes as boundary and initial conditions for global LNS and PSE calculations, respectively, we showed that the PSE solutions contain contributions from modes other than the primary mode defined by the initial conditions but do not accurately capture the full downstream response, as predicted by the theory.

Other methods exist that do not suffer from these limitations, but with the trade-off of greater computational cost. Global LNS methods can in principle capture the full linear response to any perturbation, but these calculations are typically orders of magnitude slower than PSE and remain challenging for multi-dimensional problems. The one-way marching technique developed by Towne and Colonius [44] offers a middle ground for slowly evolving flows; it can accurately evolve *all* downstream-traveling disturbances for a computational cost much less than global LNS methods but still greater than PSE. This approach was shown to correctly capture the full downstream response to the two Kelvin–Helmholtz modes for the dual-stream jet.

Acknowledgements A.T. gratefully acknowledges support from NASA Grant No. NNX15AU93A. G.R. and T.C. acknowledge support from ONR Grant N00014-16-1-2445 and The Boeing Company under Strategic Research and Development Relationship Agreement CT-BA-GTA-1.

References

1. Andersson, P., Henningson, D., Hanifi, A.: On a stabilization procedure for the parabolic stability equations. J. Eng. Mech. **33**, 311–332 (1998)
2. Andersson, P., Berggren, M., Henningson, D.S.: Optimal disturbances and bypass transition in boundary layers. Phys. Fluids **11**(1), 134–150 (1999)
3. Batchelor, G.K., Gill, A.E.: Analysis of the stability of axisymmetric jets. J. Fluid Mech. **14**(4), 529–551 (1962)
4. Bertolotti, F., Herbert, T.: Analysis of the linear stability of compressible boundary layers using the pse. Theor. Comput. Fluid Dyn. **3**(2), 117–124 (1991)
5. Bertolotti, F., Herbert, T., Spalart, P.: Linear and nonlinear stability of the Blasius boundary layer. J. Fluid Mech. **242**, 441–474 (1992)
6. Bouthier, M.: Stabilité linéaire des écoulements presque parallèles. J. de Mec. **11**, 599–621 (1972)
7. Brès, G.A., Bose, S., Emory, F. M Ham, Schmidt, O.T., Rigas, G., Colonius, T.: Large-eddy simulations of co-annular turbulent jet using a Voronoi-based mesh generation framework. In: AIAA Paper #2018-3302 (2018a)
8. Brès, G.A., Jordan, P., Le Rallic, M., Jaunet, V., Cavalieri, A.V.G., Towne, A., Lele, S.K., Colonius, T., Schmidt, O.T.: Importance of the nozzle-exit boundary-layer state in subsonic turbulent jets. J. Fluid Mech. **851**, 83–124 (2018)
9. Chang, C., Malik, M., Erlebacher, G., Hussaini, M.Y.: Compressible stability of growing boundary layers using parabolized stability equations. In: 22nd Fluid Dynamics, Plasma Dynamics and Lasers Conference, Honolulu, HI, USA (1991)
10. Cheung, L., Lele, S.: Aeroacoustic noise prediction and the dynamics of shear layers and jets using the nonlinear parabolized stability equations. Technical report TF-103 (2007)
11. Cheung, L., Lele, S.: Linear and nonlinear processes in two-dimensional mixing layer dynamics and sound radiation. J. Fluid Mech. **625**, 321–351 (2009)
12. Crighton, D.G., Gaster, M.: Stability of slowly diverging jet flow. J. Fluid Mech. **77**, 397–413 (1976)
13. Day, M., Mansour, N., Reynolds, W.: Nonlinear stability and structure of compressible reacting mixing layers. J. Fluid Mech. **446**, 375–408 (2001)
14. Fedorov, A.: Transition and stability of high-speed boundary layers. Annu. Rev. Fluid Mech. **43**, 79–95 (2011)
15. Gaster, M.: On the effects of boundary-layer growth on flow stability. J. Fluid Mech. **66**(3), 465–480 (1974)
16. Gudmundsson, K., Colonius, T.: Instability wave models for the near-field fluctuations of turbulent jets. J. Fluid Mech. **689**, 97–128 (2011)
17. Hack, M., Moin, P.: Algebraic disturbance growth by interaction of orr and lift-up mechanisms. J. Fluid Mech. **829**, 112–126 (2017)
18. Haj-Hariri, H.: Characteristics analysis of the parabolized stability equations. Stud. Appl. Math. **92**(1), 41–53 (1994)
19. Herbert, T.: Parabolized stability equations. In: AGARD-R-793 Special Course on Progress in Transition Modelling (1994)
20. Herbert, T.: Parabolized stability equations. Annu. Rev. Fluid Mech. **29**, 245–283 (1997)
21. Huerre, P., Monkewitz, P.A.: Local and global instabilities in spatially developing flows. Annu. Rev. Fluid Mech. **22**, 473–537 (1990)

22. Jordan, P., Colonius, T.: Wave packets and turbulent jet noise. Annu. Rev. Fluid Mech. **45**, 173–195 (2013)
23. Jordan, P., Colonius, T., Bres, G.A., Zhang, M., Towne, A., Lele, S.: Modeling intermittent wavepackets and their radiated sound in a turbulent jet. Technical report. In: Proceedings of the Center for Turbulence Research summer program (2014)
24. Kreiss, H., Lorenz, J.: Initial-Boundary Problems and the Navier-Stokes. Equation Classics in Applied Mathematics. Society for Industrial and Applied Mathematics, Philadelphia (2004)
25. Li, F., Malik, M.R.: On the nature of PSE approximation. Theoret. Comput. Fluid Dyn. **8**, 253–273 (1996)
26. Li, F., Malik, M.R.: Spectral analysis of the parabolized stability equations. Comput. Fluids **26**(3), 279–297 (1997)
27. Malik, M., Li, F., Chang, C.L.: Crossflow disturbances in three-dimensional boundary layers: nonlinear development, wave interaction and secondary instability. J. Fluid Mech. **268**, 1–36 (1994)
28. Paredes, P., Choudhari, M.M., Li, F.: Transition due to streamwise streaks in a supersonic flat plate boundary layer. Phys. Rev. Fluids **1**(8), 083,601 (2016)
29. Pralits, J.O., Airiau, C., Hanifi, A., Henningson, D.S.: Sensitivity analysis using adjoint parabolized stability equations for compressible flows. Flow Turbul. Combust. **65**(3–4), 321–346 (2000)
30. Ran, W., Zare, A., Hack, M., Jovanović, M.: Low-complexity stochastic modeling of spatially-evolving flows. Technical report. In: Proceedings of the Center for Turbulence Research summer program (2016)
31. Rigas, G., Colonius, T., Beyar, M.: Stability of wall-bounded flows using one-way spatial integration of Navier-Stokes equations. In: AIAA Paper #2017-1881 (2017a)
32. Rigas, G., Schmidt, O.T., Colonius, T., Brès, G.A.: One way Navier-Stokes and resolvent analysis for modeling coherent structures in a supersonic turbulent jet. In: AIAA Paper #2017-4046 (2017b)
33. Rodríguez, D., Jotkar, M.R., Gennaro, E.M.: Wavepacket models for subsonic twin jets using 3d parabolized stability equations. Compt. Rend. Mècanique **346**(10), 890–902 (2018). **(jet noise modelling and control/Modélisation et contrôle du bruit de jet)**
34. Saric, W.S., Reed, H.L., Kerschen, E.J.: Boundary-layer receptivity to freestream disturbances. Annu. Rev. Fluid Mech. **34**(1), 291–319 (2002)
35. Schmid, P.J., Henningson, D.S.: Stability and Transition in Shear Flows, vol. 142. Springer, Berlin (2001)
36. Schmidt, O.T., Towne, A., Colonius, T., Cavalieri, A.V.G., Jordan, P., Brès, G.A.: Wavepackets and trapped acoustic modes in a turbulent jet: coherent structure eduction and global stability. J. Fluid Mech. **825**, 1153–1181 (2017)
37. Sinha, A., Rodriguez, D., Bres, G., Colonius, T.: Wavepacket models for supersonic jet noise. J. Fluid Mech. **742**, 71–95 (2014)
38. Sinha, A., Gaitonde, D., Sohoni, N.: Parabolized stability analysis of dual-stream jets. In: AIAA Paper #2016-3057 (2016)
39. Tam, C.K.W., Hu, F.Q.: On the three families of instability waves of high-speed jets. J. Fluid Mech. **201**, 447–483 (1989)
40. Tempelmann, D., Hanifi, A., Henningson, D.S.: Spatial optimal growth in three-dimensional boundary layers. J. Fluid Mech. **646**, 5–37 (2010)
41. Towne, A.: Advancements in jet turbulence and noise modeling: accurate one-way solutions and empirical evaluation of the nonlinear forcing of wavepackets. PhD thesis, California Institute of Technology (2016)
42. Towne, A., Colonius, T.: Improved parabolization of the Euler equations. In: AIAA Paper #2013-2171 (2013)
43. Towne, A., Colonius, T.: Continued development of the one-way Euler equations: application to jets. In: AIAA Paper #2014-2903 (2014)
44. Towne, A., Colonius, T.: One-way spatial integration of hyperbolic equations. J. Comput. Phys. **300**, 844–861 (2015)
45. Towne, A., Cavalieri, A.V.G., Jordan, P., Colonius, T., Schmidt, O., Jaunet, V., Brès, G.A.: Acoustic resonance in the potential core of subsonic jets. J. Fluid Mech. **825**, 1113–1152 (2017)
46. Zhang, X.C., Ran, L.K., Sun, D.J., Wan, Z.H.: Optimal 'quiet' inlet perturbation using adjoint-based PSE in supersonic jets. Fluid Dyn. Res. **50**(4), 045,504 (2018)